



Cite this: *J. Mater. Chem. C*, 2025,
13, 22491

Conductive hydrogel-based epidermal electrodes for electrophysiological monitoring

Jiawei Yang,^{ab} Yi Liu,^{ab} Wenqing Yan,^{ab} Pengcheng Zhou,^{ab} Zonglei Wang,^{ab} Yuli Wang,^{ab} Yujie Zhang,^{ab} Zongman Zhang,^{ab} Fan Mo,^c Zichong Ji,^{ab} Hossam Haick  ^b and Yan Wang  ^{ab}

Electrophysiological signals generated by human physiological processes offer critical insights for health monitoring and disease diagnosis, with their precise acquisition depending on high-performance electrodes. Conductive hydrogel-based epidermal electrodes, owing to their superior properties, demonstrate significant promise in electrophysiological monitoring. This review presents a comprehensive summary of the recent progress in the design and application of conductive hydrogels for epidermal electrophysiological electrodes. It first categorizes the various types of conductive hydrogel materials, highlighting recent advancements and their unique advantages as electrode interfaces. Subsequently, the key properties of conductive hydrogel-based epidermal electrodes are discussed, including conductivity, adhesion, stretchability, and gas-permeability. Then, state-of-the-art applications across multiple electrophysiological domains are introduced, ranging from electrocardiography, electromyography, electrooculogram, and electroencephalography. Finally, a conclusion and future directions for the conductive hydrogel-based epidermal electrodes in electrophysiological monitoring are provided.

Received 12th May 2025,
Accepted 4th August 2025

DOI: 10.1039/d5tc01896j

rsc.li/materials-c

1. Introduction

Electrophysiological signals, including electrocardiogram (ECG), electromyogram (EMG), electroencephalogram (EEG), and electrooculogram (EOG), reflect critical human physiological processes, capturing bioelectric activity from heartbeats, muscle contractions, and neural functions.¹ These signals are essential for diagnosing and monitoring cardiovascular conditions,^{2,3} investigating neurological disorders,^{4,5} supporting motor rehabilitation,^{6,7} and advancing human-computer interaction systems.^{8,9} Characterized by high temporal and spatial complexity, these signals exhibit amplitudes ranging from microvolts to millivolts and frequencies spanning sub-hertz to hundreds of hertz.¹⁰ Consequently, skin-mountable electrodes, as the cornerstone of electrophysiological signal acquisition, must combine high sensitivity, mechanical stability, stretchability, and conformal skin contact to maintain signal fidelity and improve clinical outcomes.^{11–15}

Electrodes are generally categorized as invasive or non-invasive and serve as critical interfaces in biochemical sensing and human health monitoring, enabling efficient transmission and transduction between biological signals and electronic systems.^{16–20} Invasive electrodes, implanted to directly interface with target tissues, yield high-resolution signals but are constrained by surgical risks and invasiveness, limiting their use in routine monitoring. Non-invasive electrodes, which capture signals through skin contact, are further divided into dry and wet electrodes. Dry electrodes, typically constructed



Yan Wang

Dr Yan Wang is currently a tenured Associate Professor at Guangdong Technion. She received her PhD in Chemical Engineering from Monash University in 2018 and completed postdoctoral training in the Department of Electrical and Electronic Engineering at the University of Tokyo in 2021. At Guangdong Technion, her group focuses on developing materials and implementing soft wearables in real-world applications for ambulatory health care and the Internet of Things.



from metals or rigid conductive materials, are valued for their reusability and ease of application but exhibit high stiffness, making it challenging to maintain intimate skin contact during dynamic deformation or movement.²¹ This often results in skin-electrode contact gaps, elevating interface impedance and diminishing the signal-to-noise ratio (SNR). Wet electrodes, such as commercial Ag/AgCl gel electrodes, utilize conductive gel to enhance skin-electrode contact for lower skin-electrode impedance, delivering high-quality signals in the short term.²² However, they typically rely on semi-liquid conductive gels, prolonged use may lead to discomfort, allergic reactions, or signal attenuation due to gel desiccation or skin irritation. Moreover, their rigidity hampers signal acquisition in dynamic settings. In recent years, advancements in flexible electronics have positioned epidermal electrodes made from flexible materials as compelling alternatives to conventional electrodes.^{23–25} With exceptional stretchability (exceeding 200% strain), skin-matched low modulus, and ultra-thin profiles, these electrodes establish soft, stable skin interfaces, markedly reducing skin contact impedance and enhancing SNR. Consequently, the development of flexible epidermal electrodes optimized for long-term, stable signal acquisition has emerged as a pivotal research priority.

Hydrogels are hydrophilic, cross-linked polymer networks that stably retain at least 10 wt% water within their three-dimensional structure.²⁶ This structure imparts exceptional biocompatibility and a low Young's modulus, rendering hydrogels ideal for skin-contact applications.^{27,28} Traditional hydrogels generally exhibit poor electrical conductivity, which impairs their ability to respond to external signals and restricts their effectiveness in electrophysiological signal acquisition. To address this, researchers have engineered conductive hydrogels by integrating conductive elements—such as conductive polymers, nanomaterials, or ions—achieving remarkable electrical performance.^{29–35} Fine-tuning the proportions of these components enables precise control over hydrogel conductivity. Furthermore, through innovative structural and chemical designs, conductive hydrogels can exhibit superior mechanical toughness, high conductivity, self-adhesion, and breathability.^{36,37}

In recent years, conductive hydrogels have attracted significant research interest due to their promising applications in bioelectronics and wearable devices.^{38–40} For example, Mo *et al.*⁴¹ reviewed recent advancements in ionic conductive hydrogels for skin sensor applications. While previous reviews have focused on specific subtypes—such as ionic liquid (IL)-based or nanomaterial-based conductive hydrogels—there remains a lack of comprehensive discussion on their role as epidermal electrodes for electrophysiological monitoring.^{25,42–44} Ding *et al.*⁴⁵ summarized the progress of conductive hydrogels in electrophysiological signal acquisition; however, a holistic review encompassing material design, performance requirements, and practical applications in electrophysiological monitoring is still lacking. Therefore, this review aims to provide a comprehensive overview of the latest research trends in conductive hydrogel-based epidermal electrodes for electrophysiological applications. We begin by systematically introducing the typical materials used in conductive hydrogels, including design strategies for electronically conductive, ionically

conductive, and hybrid conductive systems. Next, we discuss the key performance requirements for conductive hydrogel epidermal electrodes, such as conductivity, adhesion, stretchability, and gas-permeability. Finally, we summarize recent advances in their application for monitoring various electrophysiological signals (Fig. 1).

2. Materials of conductive hydrogel-based epidermal electrodes

Conductive hydrogels are composed of selectively introduced conductive fillers embedded in a cross-linked hydrophilic polymer matrix. Based on this fabrication method and configuration, we divide the epidermal electrodes based on conductive hydrogels into three categories: ionically conductive materials, electronically conductive materials, and hybrid conductive systems. In this section, we will discuss the representative materials of these three conductive hydrogel-based epidermal electrodes.

2.1. Ionically conductive hydrogel-based epidermal electrodes

Hydrogels, composed of one or more hydrophilic polymers, can absorb and retain significant amounts of water within their three-dimensional network structure.⁵⁰ Leveraging the intrinsic hydrophilicity of hydrogel networks and the high mobility of ions in aqueous environments, ionically conductive hydrogels are typically formed by incorporating mobile ions into a crosslinked, water-rich polymer matrix. These hydrogels conduct electricity through the transport of ions such as Na^+ , K^+ , and Cl^- within the hydrated phase, which serves as the primary conduction medium. Under an applied electric field, the ions migrate through the network, enabling efficient ionic conduction.⁵¹ Ion-conductive hydrogels are classified into three typical conductive mechanisms according to the migration mode of charge carriers and the characteristics of the conductive path: electrolyte-based, poly-electrolyte-based, and IL-based.⁵² In electrolyte-based hydrogels, ionic conductivity results from the migration of small, dissociated ions (e.g., Na^+ , Cl^-) through the water-rich polymer network. These ions—introduced by dissolving inorganic salts or acids—can migrate freely within the hydrated phase when an electric field is applied. Electrolyte-based hydrogels are typically formulated by embedding these electrolytes into the polymer matrix, with commonly used examples including sodium chloride (NaCl), potassium chloride (KCl), lithium chloride (LiCl), sodium sulfate (Na_2SO_4), potassium dihydrogen phosphate (KH_2PO_4), tetramethylammonium chloride (TMACl), lactic acid, and various citrate salts.⁴¹

Among typical chlorides, LiCl as a dopant can impart high conductivity to hydrogels, which significantly reduces skin contact impedance and enables the acquisition of high-quality biopotential signals. Meanwhile, the introduction of ions can enhance the water retention of hydrogels, which is crucial for achieving long-term stable monitoring of biopotential signals.⁵³ A typical example is that Li *et al.*⁵⁴ designed a body temperature-triggered adhesive ionic conductive hydrogel based on biocompatible polyacrylamide (PAM), gelatin, LiCl, and sodium alginate



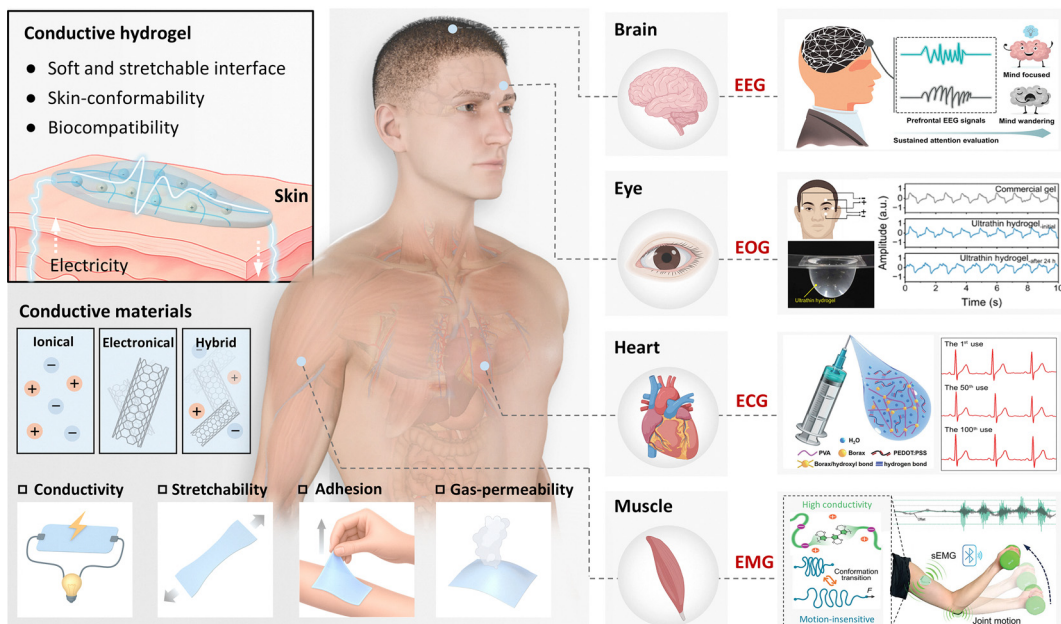


Fig. 1 Schematic interpretation of conductive hydrogel-based epidermal electrodes for electrophysiological monitoring. The left side illustrates representative types of conductive hydrogel materials, including ionic-based, electronic-based, and hybrid-based, along with their key properties, such as electrical conductivity, stretchability, adhesion, and gas permeability. The right side exhibits representative examples of electrophysiology monitoring, including ECG, EMG, EEG, and EOG. Reproduced with permission.^{46,47} Copyright 2023, 2025, Wiley-VCH. Reproduced with permission.⁴⁸ Copyright 2024, Springer Nature. Reproduced with permission.⁴⁹ Copyright 2024, American Association for the Advancement of Science.

(SA) (PGS hydrogel). Li^+ can freely shuttle within the network structure of the PGS hydrogel, and the flow of these ions imparts conductivity to the hydrogel (Fig. 2a). The conductivity of the PGS hydrogel significantly increases with increasing LiCl content, rising from 0.28 ± 0.01 to $5.69 \pm 0.20 \text{ S m}^{-1}$ (Fig. 2b). Furthermore, the conductivity of the PGS hydrogel remains largely stable under various stretching conditions (Fig. 2c). Even when the PGS hydrogel is stretched by 20% strain, the brightness of a light-emitting diode connected to it remains nearly unchanged. This demonstrates the stable conductivity of the PGS hydrogel in complex environments, facilitating high-quality electrophysiological monitoring.

Polyelectrolytes serving as ionically conductive fillers bear covalently bound ionic groups (e.g., $-\text{COO}^-$, $-\text{SO}_3^-$) along the polymer backbone. In polyelectrolyte-based hydrogels, conductivity arises primarily from the migration of mobile counter-ions (e.g., Na^+ , K^+) via ion hopping and segmental motion within the hydrated network.^{55,56} These hydrogels offer good mechanical strength, especially in double-network structures, and their conductivity can be tuned by adjusting polymer concentration, cross-linking density, and counterion type, making them suitable for hydrated and physiological conditions. Typical polyelectrolyte fillers in hydrogels include polyacrylic acid (PAA) and its derivatives, chitosan, SA, etc.⁵² Lu *et al.*⁵⁷ developed a double-network (DN) polyelectrolyte hydrogel, integrating polymer chain entanglement, chemical crosslinking, and multiple strong and weak intermolecular interactions. The hydrogel consists of a PAM network and a polyelectrolyte network composed of polyelectrolytes (poly(diallyldimethylammonium chloride)) and poly(diallyldimethylammonium chloride) (Fig. 2d). The mechanical properties and

adhesive strength of polyelectrolyte DN hydrogels can be customized by modulating the proportions of PAM, polyelectrolyte, and cosolvent. The optimal formulation yields a tensile modulus of 10.8 kPa, a tensile strain at break of 1000% strain, and an adhesive strength of 37.8 kPa. Furthermore, the stability of the crosslinked PAM network, combined with the unique properties of polyelectrolytes that induce phase separation, ensures the hydrogel's stability even in salt solutions while exhibiting solvent-tunable transparency (Fig. 2e). Owing to the presence of polyelectrolytes, the hydrogel exhibits excellent conductivity. This conductive hydrogel can be stretched up to 1100% strain before reaching its breaking point while maintaining stable conductivity even under high tensile strain (Fig. 2f).

IL-based hydrogels incorporate room-temperature ILs—such as 1-ethyl-3-methylimidazolium bis(trifluoromethanesulfonyl)-imide (EMIM-TFSI)—either as co-solvents or as dispersed conductive media within the hydrogel network. Their ionic conductivity stems from the unrestricted movement of both organic cations and anions, which act as charge carriers. These hydrogels exhibit high and humidity-independent ionic conductivity, excellent electrochemical stability, and strong anti-freezing and anti-drying properties. They are particularly suitable for long-term use in harsh environments and maintain good flexibility and thermal stability.^{58,59} By polymerizing IL monomers into PIL, the inherent properties of IL can be transferred to the polymer chain, thereby obtaining ionic conductive hydrogels with high conductivity. Zhao *et al.*⁶⁰ prepared an ionic gel through one-step photoinitiated polymerization of 2,2,2-trifluoroethyl acrylate and N-isopropylacrylamide (NIPAm) in the hydrophobic ILs 1-ethyl-3-methylimidazolium



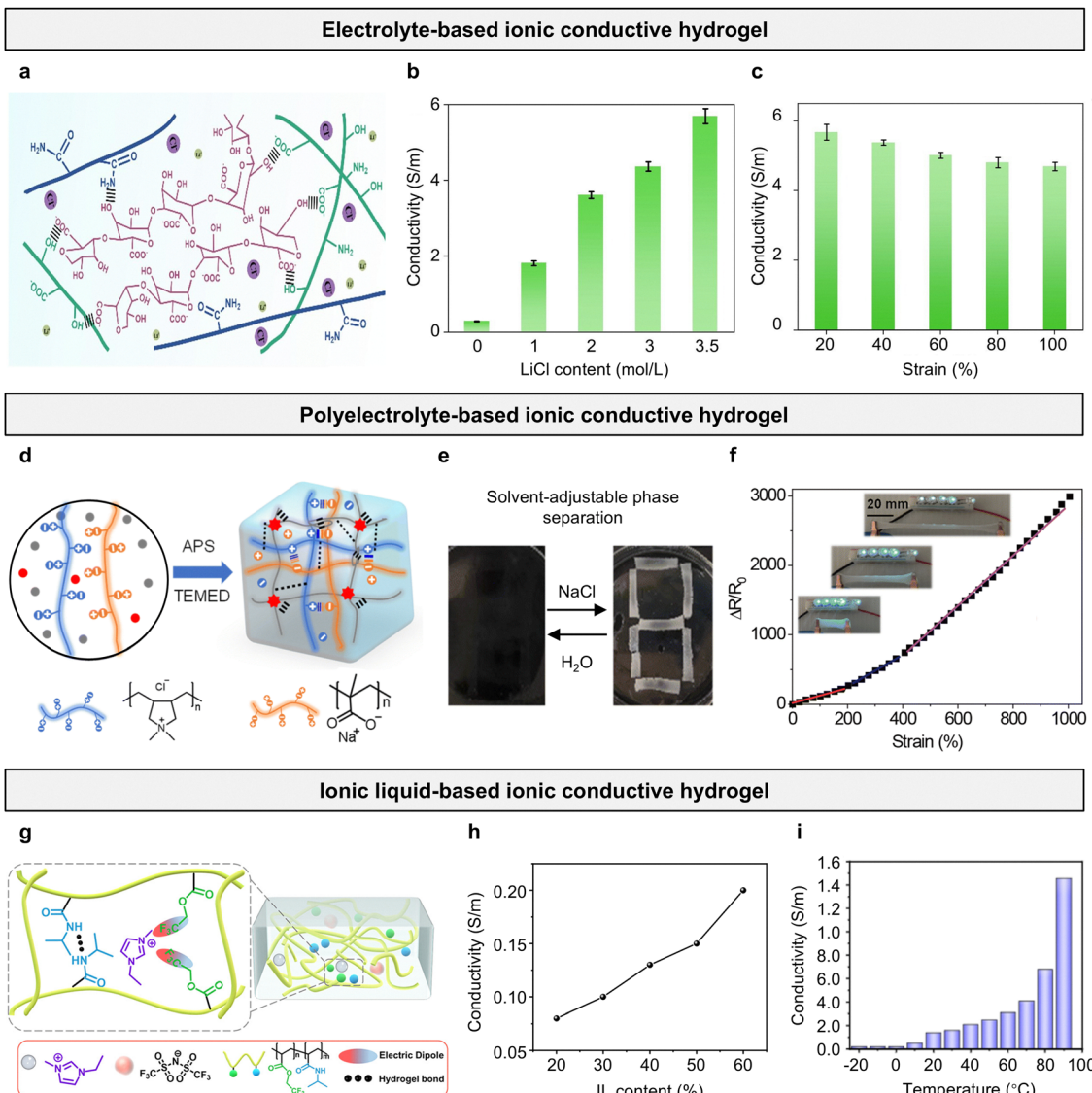


Fig. 2 Ionically conductive hydrogel-based epidermal electrodes. (a) PGS conductive hydrogel and its network structure. (b) Conductivity of PGS hydrogels with different LiCl contents. (c) Conductivity of PGS hydrogel under different strain. Reproduced with permission.⁵⁴ Copyright 2024, Elsevier. (d) Schematic diagram of the polyelectrolyte hydrogel preparation and structure. (e) The photograph illustrates the solvent-tunable transparency of the hydrogel electrolyte under induced phase separation. (f) Tensile strain induced relative resistance changes of the hydrogel. Reproduced with permission.⁵⁷ Copyright 2025, Royal Society of Chemistry. (g) Schematic diagram of the structure of the ionogel. (h) Conductivity of ionogel with different IL contents. (i) The ionic conductivities of the ionogel in the temperature range from -20 to 90 $^{\circ}\text{C}$. Reproduced with permission.⁶⁰ Copyright 2023, American Chemical Society.

bis(trifluoromethylsulfonyl)imide ([EMIm][TFSI]) (Fig. 2g). The ionic gel demonstrates exceptional transparency (94.8%), underwater self-healing capability (up to 96%), toughness (3.93 MJ m^{-3}), and underwater adhesion strength (102.77 ± 2.4 kPa). As the ILs mass percentage increased from 20% to 60%, the ionic gel's conductivity surged from 8.15×10^{-4} to 2.04×10^{-3} S cm^{-1} (Fig. 2h). Inspired by the excellent temperature responsiveness of ILs, the temperature sensitivity of the ionic gel was further characterized. Across a wide temperature range of -20 to 90 $^{\circ}\text{C}$, the ionic gel exhibited high ionic conductivity (2×10^{-4} to 1.45×10^{-2} S cm^{-1}). Due to increased ion mobility, the ionic conductivity sharply increased with rising temperature (Fig. 2i).

2.2. Electronically conductive hydrogel-based epidermal electrodes

In electronically conductive hydrogel-based epidermal electrodes, the hydrogel matrix provides a soft, biocompatible scaffold, while embedded conductive materials enable efficient electron transport. Electrical conduction is achieved by incorporating intrinsically conductive components into the hydrogel network. These materials form continuous pathways that support charge transport through electron hopping or band-like conduction. The conductivity depends on factors such as filler dispersion and connectivity, polymer crystallinity, doping level, and interfacial interactions.^{61,62} Electron conduction primarily

encompasses three categories: (i) conductive polymers, including poly(3,4-ethylenedioxythiophene)polystyrene sulfonate (PEDOT:PSS), polypyrrole (PPy), and polyaniline (PANI);^{63,64} (ii) carbon filler-based nanomaterials, such as carbon nanotubes (CNTs) and graphene oxide (GO);^{65,66} and (iii) metal-filler nanoparticles, such as silver nanoparticles (AgNPs).^{67,68} Incorporating these materials into hydrogels yields electron-conductive hydrogels with enhanced performance. A typical example is that Huang *et al.*⁶⁹ utilized PEDOT:PSS to promote the self-polymerization of zwitterionic [2-(methacryloyloxy)ethyl]dimethyl-(3-sulfopropyl) (SBMA), proposing an *in situ* formed conductive hydrogel (PSP) (Fig. 3a).

This hydrogel exhibits exceptional elasticity (elastic recovery rate > 96%), robust adhesion strength (6.5 kPa), biocompatibility, and intrinsic antibacterial properties. The gelation process generates minimal heat (< 5 °C), enabling *in situ* formation on the skin. Furthermore, the hydrogel achieves intimate skin contact, creating a highly conformal interface (Fig. 3b). The PSP hydrogel exhibits high conductivity, attributed to its polycrystalline ionic network and conductive PEDOT:PSS. As the SBMA content increases, electronic conductivity of the PSP hydrogel decreases from 0.08 to 0.03 S m⁻¹, respectively. This reduction is attributed to the higher solid content and intensified inter- and intra-chain

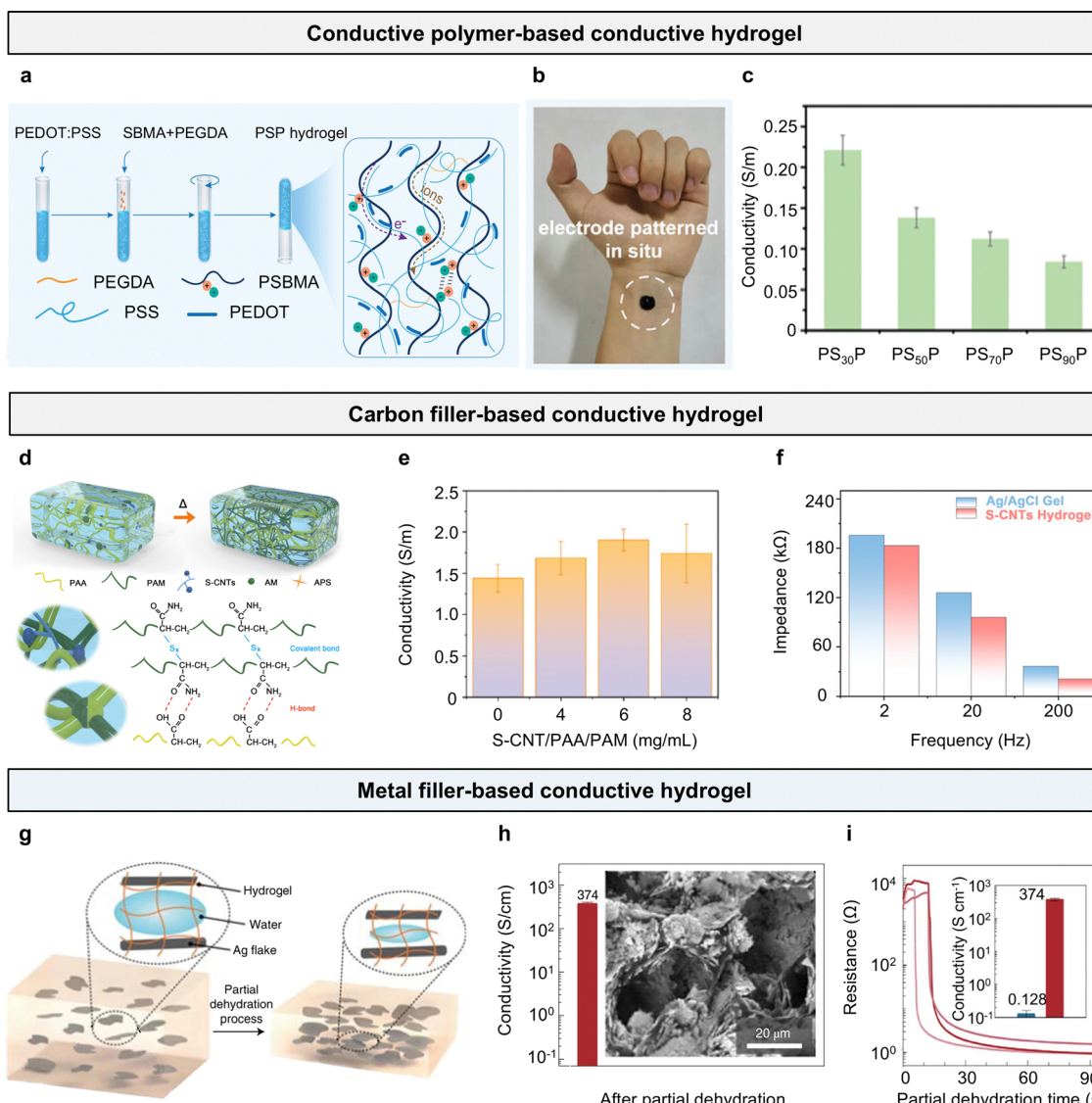


Fig. 3 Electronically conductive hydrogel-based epidermal electrodes. (a) Schematic diagram of the fabrication and promising applications of PSP hydrogel. (b) Photographs shows that the PSP hydrogel can be patterned on skin *in situ*. (c) The conductivity of the PSP hydrogel with different SBMA content. Reproduced with permission.⁶⁹ Copyright 2023, Wiley-VCH. (d) Schematic illustration of the preparation process of the S-CNTs/PAA/PAM hydrogel. (e) Conductivity of the prepared hydrogel with different S-CNTs content. (f) Impedance comparison at various frequencies of the S-CNTs/PAA/PAM hydrogel and commercial Ag/AgCl gel electrodes. Reproduced with permission⁷⁰ Copyright 2025, American Chemical Society. (g) Composition of the conductive hydrogel composite composed of micrometre-scale Ag flakes and PAM-alginate hydrogel (Ag-hydrogel composite). (h) Conductivity of the Ag-hydrogel composite after the controlled partial dehydration process. (i) Conductivity of the Ag-hydrogel composite and micrographs of the composite after the controlled partial dehydration process. Reproduced with permission.⁷¹ Copyright 2021, Nature Publishing Group.



electrostatic interactions, which impede the formation of efficient conductive pathways. Nevertheless, the PSP hydrogel retains high conductivity, fully meeting the requirements for EMG monitoring (Fig. 3c).

Dai *et al.*⁷⁰ developed a hydrogel-based epidermal electrode composed of graphene nanoplates, PAA, and PAM (S-CNTs/PAA/PAM). S-CNTs, enriched with graphene nanoplates, are synthesized *via* a two-step sulphuration process employing thiourea and dibenzyl disulfide (Fig. 3d). The incorporation of sulfur atoms strengthens the interfacial interactions between S-CNTs and PAA/PAM through C-S covalent bonding, significantly improving the hydrogel's mechanical performance ($>1200\%$ strain) and electrical conductivity (1.9 S m^{-1}). The incorporation of S-CNTs enhances the conductivity of PAA/PAM hydrogels to a certain extent. The 6S-CNTs/PAA/PAM hydrogel exhibits a conductivity of 1.9 S m^{-1} , surpassing that of the pristine PAA/PAM hydrogel (1.44 S m^{-1}). The unique chain structure of S-CNTs on the polymer chains shortens the charge migration pathway, thereby increasing the migration rate and improving conductivity. However, excessive addition of S-CNTs leads to them aggregation, which increases the overall resistance of the hydrogel and results in reduced conductivity (Fig. 3e). Moreover, the S-CNTs/PAA/PAM hydrogel, employed as an epidermal electrode for electrophysiological signal acquisition, demonstrates significantly lower skin-contact impedance than commercial Ag/AgCl gel electrodes across the $1\text{--}10^5\text{ Hz}$ range (Fig. 3f).

Yunsik *et al.*⁷¹ designed a highly conductive, flexible hydrogel-based epidermal electrode by embedding micron-scale Ag particles

within a PAM-alginate hydrogel matrix. A critical step in achieving high conductivity involves partial dehydration of the hydrogel matrix, facilitating the formation of percolation pathways by Ag flakes. Prior to partial dehydration, the Ag-hydrogel composite exhibits ionic conductivity with a low conductivity of $\sim 0.13\text{ S cm}^{-1}$. At this stage of the fabrication process, the volume fraction of Ag fillers (5 vol%) is insufficient to achieve percolation. Subsequently, the conductivity of the composite increases significantly from 0.12 to 374 S cm^{-1} following dehydration (Fig. 3h). During the partial dehydration process, Ag-hydrogel composites with varying amounts of Ag added *in situ* yielded the resistance values of the hydrogel. The resistance of the Ag-hydrogel composite decreased exponentially after drying for 10–15 minutes, stabilizing at $1.14 \pm 0.35\text{ }\Omega$ after 90 minutes, with a corresponding volume conductivity of $374 \pm 30.8\text{ S cm}^{-1}$ (Fig. 3i).

2.3. Hybrid conductive hydrogel-based epidermal electrodes

Hybrid conductive hydrogels combine ionic and electronic conductive components within a single network, effectively addressing the limitations of pure systems. Ionically conductive hydrogels offer good biocompatibility and flexibility but often exhibit reduced conductivity under low humidity or freezing conditions. In contrast, electronically conductive hydrogels provide stable and high conductivity but may compromise stretchability and lack sufficient ionic transport. By integrating both mechanisms, hybrid hydrogels form synergistic, bicontinuous ion-electron conduction networks that enhance charge transport kinetics and conductivity stability. This dual-conduction design

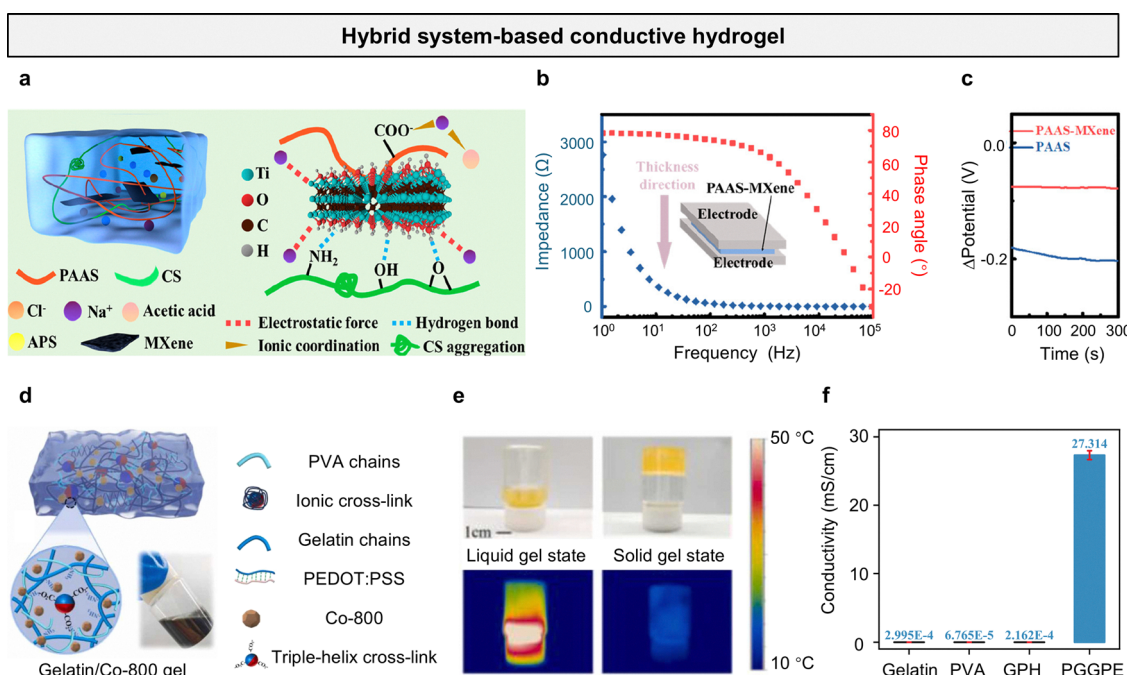


Fig. 4 Hybrid conductive-based conductive hydrogel. (a) Composition of PAAS-MXene cross-linked by single-layer MXene. (b) Electrical impedance of Bode plot in the thickness direction of PAAS-MXene hydrogel. (c) Comparison of polarization potential values and polarization potential change values of PAAS and PAAS-MXene. Reproduced with permission.⁷³ Copyright 2022, American Chemical Society. (d) Schematic illustration of the multifunctional bio-hydrogel. (e) Conductivity of gelatin, PVA, GPH, and PEDOT:PSS/graphene/gelatin/PVA hydrogel. (f) Comparison of single heartbeat waveform recorded by hydrogel electrode and commercial electrode. Reproduced with permission.⁷⁴ Copyright 2023, Wiley-VCH.



enables the hydrogel to maintain performance under mechanical deformation, temperature variation, and environmental stress. Additionally, hybrid networks allow tunable physical and electrical properties through molecular and structural engineering, such as tailoring polymer composition, conductive filler distribution, or crosslinking strategies.⁷² For example, Luo *et al.*⁷³ designed an MXene-induced crosslinking fast-gelling hybrid conductive hydrogel electrode (PAAS) composed of acrylamide, NaCl, and MXene (Fig. 4a). Under the initiation of ammonium persulfate (APS), the C=C bonds of sodium acrylate are opened for polymerization, and then MXene acts as a crosslinker to rapidly form polymer chains. Meanwhile, the introduction of MXene increases the hydrogel's conductivity (2.3 S m^{-1}). In this system, sodium ions from NaCl and poly (sodium acrylate) impart ionic conductivity to hydrogel, while also establishing electrostatic interactions with MXene and forming ionic coordination with acetic acid used for dissolving chitosan. Due to the addition of negatively charged MXene, the directional alignment of positively charged chitosan and sodium ions under an external electric field is restricted, reducing the hydrogel's polarization potential (change rate less than $6.5 \times 10^{-4} \text{ V min}^{-1}$) (Fig. 4b and c).

Wang *et al.*⁷⁵ developed a hybrid conductive hydrogel leveraging the synergistic effects of PEDOT:PSS/graphene and Na^+ ions (Fig. 4d). The hydrogel (GPH), composed of a dual-crosslinked network of gelatin and polyvinyl alcohol (PVA), exhibits a unique thermally responsive reversible phase transition between a flowable fluid state and a viscoelastic gel state (Fig. 4e). Compared to pristine hydrogels ($6.76 \times 10^{-5} \text{ mS cm}^{-1}$), the conjugated structure of PEDOT:PSS in the hybrid conductive hydrogel facilitates electron mobility, while graphene sheets form a conductive network that supports efficient electron and ion transport. This results in significantly enhanced electrical conductivity, reaching 27.31 S cm^{-1} (Fig. 4f).

3. Properties of conductive hydrogel-based epidermal electrodes

To fulfill the essential requirements for electrophysiological signal monitoring, conductive hydrogel-based epidermal electrodes can be engineered with tailored properties, including conductivity, stretchability, and adhesion, using diverse synthesis and fabrication techniques (Table 1). This section outlines the essential properties required for conductive hydrogel epidermal electrodes, highlighting their critical role in ensuring the efficacy and reliability of electrophysiological monitoring.

3.1. Conductivity

The conductivity of hydrogel-based epidermal electrodes significantly influences the performance of bioelectronic interface electrodes, crucial for enabling efficient electrical signal transmission between biological tissues and electronic components while ensuring stable electrophysiological communication.¹⁰¹ The polymer network serves as a structural scaffold, while the conductive fillers confer electrical conductivity to the hydrogel.^{32,102} To date, a range of conductive materials, encompassing both electronic and ionic

conductive fillers, have been employed in the fabrication of conductive hydrogels for epidermal electrodes.¹⁰²

Ionic conductive fillers are incorporated into hydrogel systems by introducing acids (e.g., HCl, H_2SO_4 , H_3PO_4), ionic compounds (e.g., LiCl, FeCl_3 , AlCl_3 , NaOH, KOH), or ionic liquids (e.g., 1-ethyl-3-methylimidazolium sulfate), which release free ions to significantly enhance electrical conductivity.^{41,103} For instance, Zhang *et al.*¹⁰⁴ prepared highly conductive hydrogels by adding KOH and NaOH to a carboxymethyl chitosan (CECT)/PAM-based hydrogel (CTA). The ionic conductivity of the hydrogel samples was measured using electrochemical impedance spectroscopy, with conductivity ranging from 0.38 to 0.62 S m^{-1} .

Another way to achieve high conductive performance is typically to incorporate electronic conductive fillers (such as intrinsically conductive polymers, metal nanoparticles, or carbon-based nanomaterials) into hydrogels.^{105,106} A typical example is that Wang *et al.*¹⁰⁷ employed a synergistic approach combining freeze-drying and salting-out treatment to prepare a conductive hydrogel composite based on silver nanowires (AgNWs) and PVA (Fig. 5a). This method successfully constructed a layered hydrogel structure and significantly enhanced the local concentration of AgNWs by inducing continuous phase separation. The resulting conductive hydrogel composite exhibited remarkable properties, including ultra-high conductivity, excellent stretchability (480% strain), and outstanding biocompatibility. The phase separation of PVA in the hydrogel evolves with the extension of the salting-out time. By optimizing the salting-out treatment time, the researchers successfully controlled the phase separation process, resulting in a hydrogel with a conductivity exceeding 1739 S cm^{-1} (Fig. 5b). Due to the high concentration of AgNWs, the prepared hydrogel still maintains high conductivity under stretching, which is superior to other types of hydrogels (Fig. 5c). Zhang *et al.*¹⁰⁸ developed a liquid metal (LM)-doped PVA-LM hydrogel, incorporating LM microdroplets within a tannic acid (TA)-modified PVA matrix (Fig. 5d). LM microdroplets were employed as crosslinkers to enhance mechanical properties while providing exceptional conductivity, reaching a peak value of $217\,895 \text{ S m}^{-1}$. The sedimentation time of LM profoundly influences the hydrogel's conductivity, with the non-sedimented PVA-LM hydrogel exhibiting a significantly lower conductivity of 0.004 S m^{-1} . After a sedimentation time of 30 minutes, the conductivity of the PVA-LM hydrogel surged by five orders of magnitude to 455 S m^{-1} , reflecting significant LM microdroplet precipitation (Fig. 5e). The PVA-LM hydrogel was subjected to resistance measurements over 1200 stretching cycles (40% strain), during which its resistance progressively decreased from 4.8 to 4.5Ω (Fig. 5f). This suggests mechanical sintering of LM microdroplets on the hydrogel surface under external forces, concurrently enhancing its conductivity.

For epidermal electrodes, both ionic and electronic conductivity are essential yet functionally distinct. Ionic conductivity plays a crucial role in interfacing with the skin, which is a naturally ionic medium. Hydrogels with high ionic conductivity can form low-impedance, conformal contacts with the stratum corneum, facilitating effective coupling with bioelectric signals such as ECG, EMG, or EEG. This enables stable, high-fidelity



Table 1 Summary of conductive hydrogel-based epidermal electrodes from different conductive mechanisms

Conductive types	Hydrogel matrix	Conductivity materials	Conductivity (test method)	Stretchability (%)	Adhesion (kPa)	Biocompatibility	Electrophysiological signals	Ref.
Ionic	AM/BIS/water	NaCl	1.3 S m ⁻¹ (EIS)	1326	14	—	ECG/EEG	76
	AAM/PEGDA/water	LiCl	0.01 S m ⁻¹ (EIS)	2500	—	—	EOG/EEG	77
	PVA/b-PEI/water	CaCl ₂	3.09 S m ⁻¹ (EIS)	1291	10	—	ECG/EMG/EEG	78
	EGDMA/water	VBIm-NTf ₂	0.0065 S m ⁻¹ (AC Resistance)	200	~400	—	ECG	79
	HEMA/SBMA/MBA/water	LiTFSI	3 S m ⁻¹ (four-point probe)	287	7.5	High	ECG/EMG	80
	PAM/PDDA/water	PMAANa	—	1000	19.2	—	ECG/EMG	57
	DMAEA/MBA/KPS/water	ZM	—	1880	400	High	ECG/EMG	81
	AAm/LMA/KPS/water	—	—	1410	—	High	ECG/EMG	82
	PVA/PAM/F-SiO ₂ /water	CaCl ₂	10.58 S m ⁻¹ (EIS)	1450	26	—	ECG/EMG	83
	Gelatin/glycerol/borax/water	Na ₂ SO ₄	9.3 S m ⁻¹ (EIS)	696	176	—	ECG/EMG/EEG/EOG	49
Electronic	Proanthocyanins/guar gum/CNF/water	FeCl ₃	0.023 S m ⁻¹ (four-point probe)	—	7.9	—	ECG/EMG	84
	EG/AAm/MBA/water	DES	1.6 S m ⁻¹ (AC resistance)	1660	0.01	High	ECG/EMG	85
	PVA/PDA/water	PEDOT:PSS	2.18 S m ⁻¹ (four-point probe)	535	197	—	EMG	86
	PDA/water	PEDOT:PSS	4 S m ⁻¹ (AC resistance)	1300	22.4	High	ECG/EMG	87
	PVA/SA/APS/FeCl ₃ /water	PEDOT:PSS	0.256 S m ⁻¹ (EIS)	334	—	—	ECG/EMG/EEG	88
	NIPAm/HEA/water	poly(Cu-arylacetylide)	3.1 S m ⁻¹ (EIS)	108	43	High	ECG/EMG	89
	APS/SA/MBAK/KCl/CaSO ₄ /water	PEDOT:PSS	—	50	64	High	EEG	90
	PAM/AM/silk fibroin/water	MXene	0.25 S m ⁻¹ (AC resistance)	1560	29	—	EMG/EOG	91
	TA/ACC/Water	LM	0.02 S m ⁻¹ (EIS)	1000	28.9	High	ECG/EMG	92
	PVA/borax/water	PEDOT:PSS	0.002 S m ⁻¹ (two-point probe)	10 000	15.7	—	ECG/EMG	93
Hybrid	PAA/AlNO ₃ /water	MXene	0.7 S m ⁻¹	2400	494.2	—	ECG/EMG	94
	PAA/PVA/water	RGO	0.11 S m ⁻¹ (-point probe)	—	5.4	High	ECG/EMG/EOG	95
	PAM/alginate/water	Ag	37 400 S m ⁻¹ (four-point probe)	250	—	—	EMG	71
	PEGDA/water	PEDOT:PSS/ SBMA	0.03 S m ⁻¹ (EIS and DC resistance)	390	6.5	High	ECG/EMG	69
	PAA/SA/AD/ADQ/water	MXene/LiCl	1.8 S m ⁻¹ (EIS)	800	~27	High	ECG	96
	HA/water/glycerin	GNs/KCl/NaCl	0.33 S m ⁻¹ (EIS)	—	~5.5	High	EEG	97
	PEDOT:PSS/Fe/water	PEDOT:PSS/Fe	1.25 S m ⁻¹ (EIS)	15	—	High	ECG	98
	PAA/TOCNFs/water	PEDOT:PSS/ Al(TFSI) ₃	7.1 S m ⁻¹ (EIS)	770	28	High	ECG/EMG	99
	PVA/water	PPy/FeCl ₃	80 S cm ⁻¹ (four-point probe)	36	—	High	EMG	100

BIS: *N,N'*-methylenebisacrylamide; PEGDA: poly(ethylene glycol)diacrylate; HEMA: 2-Hydroxyethyl methacrylate; SBMA: [2-(Methacryloxy)ethyl]dimethyl-(3-sulfo-propyl)ammonium hydroxide; MBA: *N,N'*-methylenebisacrylamide; SBMA: zwitterionic [2-(methacryloyloxy)ethyl]dimethyl-(3-sulfopropyl); LiTFSI: bis(trifluoromethanesulfonimide) lithium salt; PDA: polydopamine; NIPAm: *N*-isopropylacrylamide; HEA: 2-hydroxyethyl acrylate; GNs: graphite nanoparticles; HA: hyaluronic acid; DMAEA: 2-(Dimethylamino)ethyl acrylate; MBA: *N,N'*-methylenebis(acrylamide); KPS: potassium persulfate; LMA: lauryl methacrylate; ACC: calcium carbonate. EIS: electrochemical impedance spectroscopy.

acquisition of weak biopotentials with reduced signal loss or distortion.

Conversely, electronic conductivity is vital for rapid and efficient transmission of the collected signals to external read-out devices. Materials such as PEDOT:PSS, CNTs, or MXene can form continuous electron pathways that minimize resistance across the electrode structure. In hybrid conductive hydrogels, the synergy between these two conduction mechanisms enables high SNR, reduced motion artifacts, and stable performance under varying environmental and mechanical conditions. By combining the skin-compatible interface of ionic systems with

the robust signal transfer capability of electronic systems, hybrid hydrogels offer a balanced and integrated solution for long-term, reliable epidermal bioelectronic applications.

3.2. Adhesion

Superior adhesive properties enable hydrogel-based epidermal electrodes to effectively adhere to the skin, minimizing skin-contact impedance and enhancing the quality and stability of monitored signals.¹⁰⁹ To enhance the adhesive properties of conductive hydrogel-based epidermal electrodes, there are three typical mechanisms to enhance the adhesiveness of



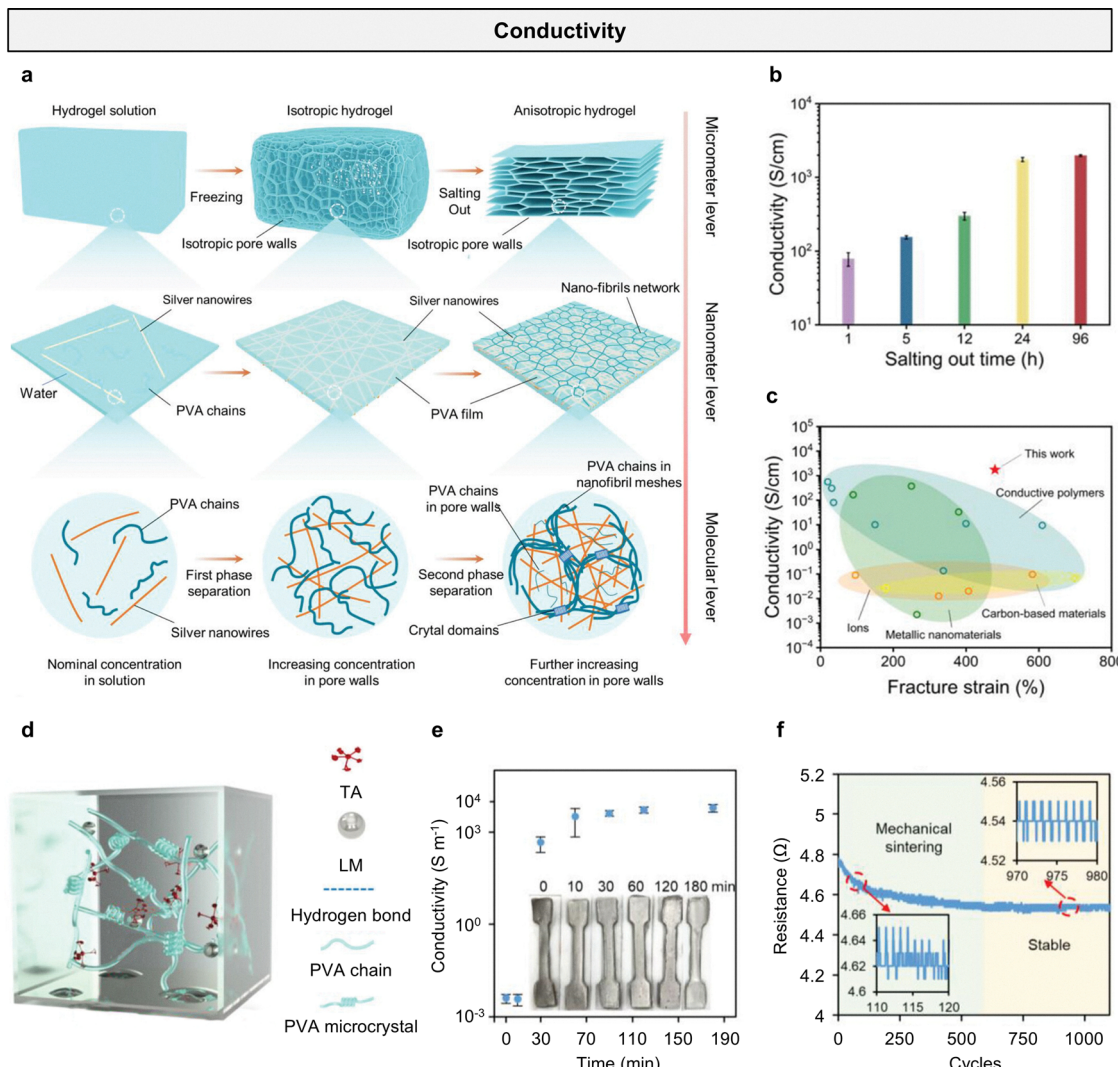


Fig. 5 Conductivity. (a) Schematic illustrating the fabrication procedure of AgNWs-PVA hydrogel composites by combining freezing and salting-out treatments. (b) Conductivity of the AgNWs-PVA hydrogel composites with varying durations of salting-out treatment. (c) Comparison of conductivity and fracture strain of the Ag-PVA hydrogel with other conductive hydrogels based on different conductive fillers. Reproduced with permission.¹⁰⁷ Copyright 2024, Wiley-VCH. (d) Schematic of PVA-LM hydrogel network. (e) Conductivity of PVA-LM hydrogels with different aging times. (f) The resistance response of PVA-LM hydrogel under cyclic stretching for 1000 cycles. Reproduced with permission.¹⁰⁸ Copyright 2024, Wiley-VCH.

conductive hydrogel epidermal electrodes: physical adhesion, chemical adhesion, and biomimetic strategies.¹¹⁰ In physical adhesion, external stimuli, including pH variations,¹¹¹ temperature fluctuations,¹¹² ultraviolet light,¹¹³ magnetic fields,¹¹⁴ and electric fields,¹¹⁵ can be utilized to modulate the adhesive properties of hydrogels. A typical example is that Liu *et al.*¹¹⁶ proposed an electro-adhesion strategy with electrically programmable strength for universal and super-strong hydrogel bonding. The hydrogel is composed of PAA-Fe-Li. Owing to the robust hydration capacity of Li^+ ions, they significantly modulate polymer chain interactions within the hydrogel, thereby enhancing its interfacial bonding through surface diffusion and accumulation (Fig. 6a). Driven solely by entropy related to the concentration gradient of the involved ions, PAA-Fe-Li exhibits effective adhesion to PVA hydrogels. After 5 seconds of contact, the adhesion strength and adhesion energy reach 0.24 MPa and

660 J m^{-2} , respectively. Subsequently, under a positive DC voltage, the adhesion efficiency of PAA-Fe-Li to PVA at ambient temperature significantly increased by ≈ 24 times (Fig. 6b). The peak adhesion strength and adhesion energy of PAA-Fe-Li with PVA substrates can reach 1.2 MPa and 3750 J m^{-2} , respectively. Adhered PAA-Fe-Li and PVA samples with a cross-sectional diameter of 6 mm can withstand at least 5 kg of weight (Fig. 6c).

In chemical adhesion, the adhesive effect is mainly caused by chemical bonding and/or non-covalent interactions between reactive groups in the hydrogel and on the skin surface.^{110,117} Covalent bonds play a predominant role in hydrogel adhesion due to their higher bond energy relative to other interactions.¹¹⁸ Non-covalent interactions, including hydrogen and ionic bonds, are extensively employed in the fabrication of adhesive hydrogels to enhance interfacial adhesion.¹²⁰ Hydrogen bonds, distinguished for their adjustable strength, biocompatibility, and

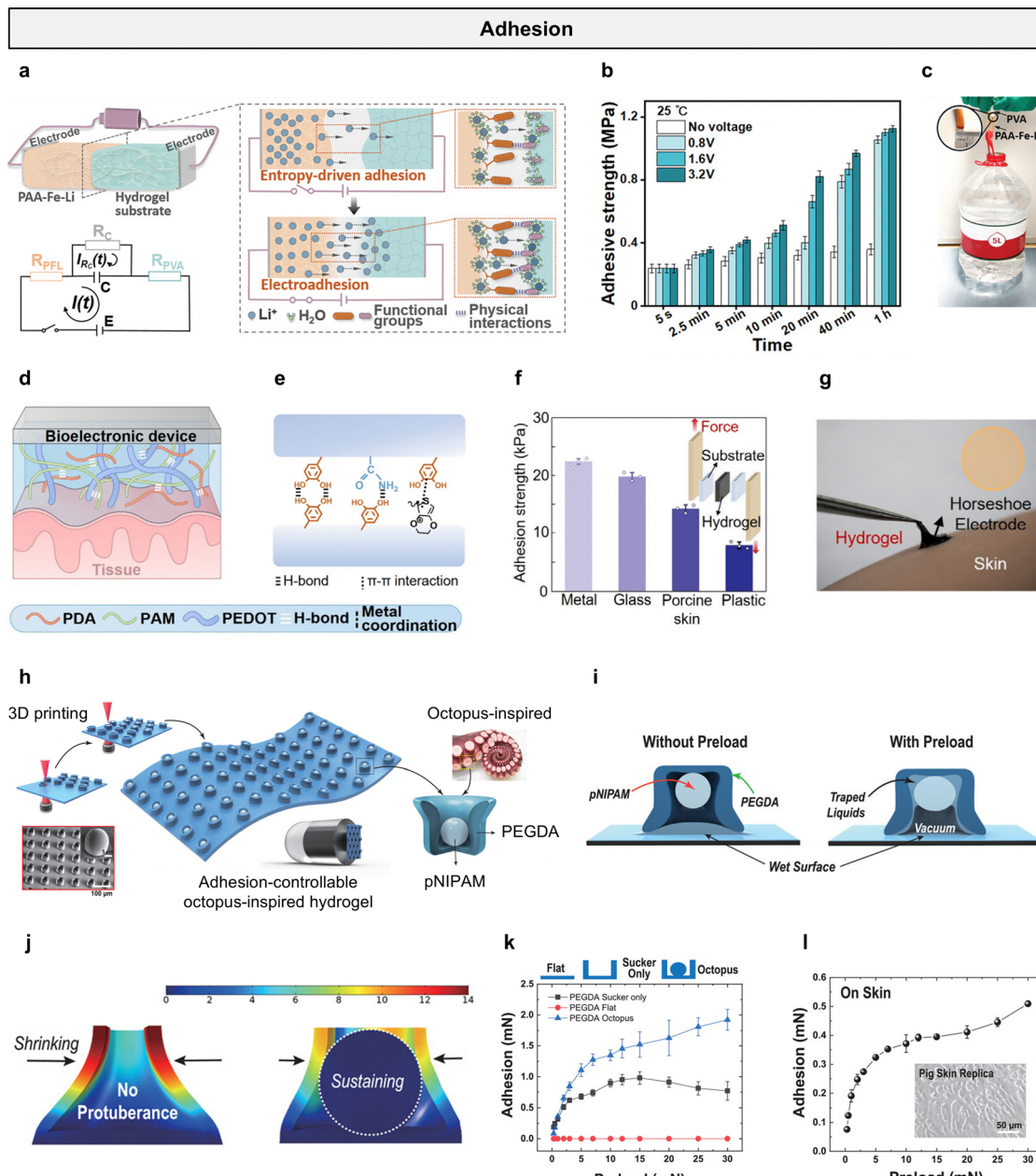


Fig. 6 Adhesion. (a) Mechanisms for strong interfacial bonding between the PAA-Fe-Li hydrogel and hydrogel substrate and schematic illustration of the proposed circuit model for electro-adhesion. (b) Adhesive strength of electro-adhesion between PAA-Fe-Li and PVA hydrogels at 25 °C. (c) Strong adhesion (> 5 kg) demonstration between PAA-Fe-Li and PVA. Reproduced with permission.¹¹⁶ Copyright 2022, Wiley-VCH. (d) Schematic illustration of a conventional bioelectronic device adhering directly to tissue. (e) Noncovalent interactions among dopamine methacrylate, PEDOT, PDA, and PAM chains. (f) Adhesion strength of hydrogel to different substrates by lap shear test. (g) Image of a hydrogel bioelectronic device for EMG and ECG monitoring. Reproduced with permission.⁸⁷ Copyright 2025, American Chemical Society. (h) Fabrication process of a polyethylene glycol diacrylate hydrogel. (i) Schematic illustration with finite element method simulation showing the adhesion mechanism of the sucker architecture with and without the inner protuberance structure. (j) Representative time-dependent profiles of adhesion results for the hydrogel patterns and flat glass for comparison. (k) Adhesion forces for different preloads (0.3–30 mN) in the samples of the inner pNIPAM and outer pNIPAM. (l) Adhesion results for different preloads (0.3 to 30 mN) in underwater conditions measured on the pig skin replica shown in inset. Reproduced with permission.¹¹⁹ Copyright 2022, Wiley-VCH.

reversible bonding capabilities, represent a key intermolecular force. Generally, individual hydrogen bonds in hydrogels are weak, necessitating their synergistic combination with other interactions or the formation of multiple hydrogen bonds to enhance adhesion.¹²¹ For example, Lao *et al.*⁸⁷ developed a

hydrogel with inherent adhesion and conductivity by integrating PAM-polydopamine (PDA) into conductive PEDOT, exhibiting a tissue-mimetic modulus (Fig. 6d). The adhesion is formed through non-covalent interactions of hydrogen bonds and π - π interactions with polydiacetylene and PAM chains (Fig. 6e). The



shear strength of the hydrogel, adhered to various substrates including metal, glass, pig skin, and plastic, was measured at 22.4, 19.8, 14.2, and 7.9 kPa, respectively (Fig. 6f). Due to its ultra-soft and strong adhesive properties, the conductive hydrogel epidermal electrode can form a tight and robust interface with human tissue, thereby reducing artifacts caused by body movement (Fig. 6g). In biomimetic structures, the adhesion mechanisms of various organisms (including tree frogs, mussels, octopuses, and geckos) have attracted numerous researchers and inspired the development of biomimetic hydrogels.^{122,123} For instance, the eight arms of an octopus are equipped with numerous suckers, each generating negative pressure *via* muscle control to produce robust adhesion.¹²⁴ This mechanism, independent of chemical adhesives, enables secure attachment to wet or irregular surfaces, such as marine rocks or prey. These attributes inspire the development of high-performance, reusable biomimetic adhesive materials tailored for complex environments. Inspired by the octopus's orifice, Lee *et al.*¹¹⁹ printed polyethylene glycol diacrylate (pNIPAM) hydrogel to form an outer wall, completing an internal dome-shaped structure mimicking octopus protrusions, which enhanced dry and wet adhesion (Fig. 6h). The pNIPAM achieves robust wet adhesion under external preload by inducing cohesive forces among liquid molecules at interacting wet surfaces (Fig. 6i and 6j). Due to the enhancement of suction, the sucker with an internal dome-like protrusion structure can enhance adhesion in wet environments (Fig. 6k). Adhesion was evaluated under preloads ranging from 0.5 to 30 mN on a skin-mimicking surface. Owing to the roughness of pig skin, adhesion on pig skin was approximately three times lower or more than that on a smooth glass surface (Fig. 6l).

3.3. Stretchability

Beyond essential conductivity and adhesion, superior tensile performance is a critical attribute that positions hydrogels as ideal materials for stretchable epidermal electrodes. This capability allows hydrogel-based electrodes to effectively accommodate body deformations while sustaining conformal contact, ensuring reliable signal transmission.²⁷ Typical strategies for enhancing the mechanical properties of hydrogel epidermal electrodes include constructing multiple crosslinked network structures, adding nanocomposites, introducing supramolecular interactions, etc.^{102,125} For example, Zhang *et al.*¹²⁶ developed an all-cellulose hydrogel with exceptional stretchability by introducing supramolecular structures through the ring-opening reaction of cellulose's anhydroglucose units *via* dehydration (Fig. 7a). The hydrogel's tensile properties were enhanced by modifying the cellulose structure and tuning interchain interactions. To increase chain flexibility, periodate oxidation was employed to selectively cleave the C2–C3 bond, converting secondary hydroxyl groups into aldehyde groups and thereby opening the anhydroglucose ring structure. The resulting hydrogel exhibited a record-breaking tensile of 42 200% strain. The mechanical properties of the hydrogel were significantly influenced by the content of diol cellulose nanorods (DCNRs). As the DCNR content increased from 23.3 to 28.8%, the tensile stress rose progressively from 7 to 25 kPa. When the DCNR content ranged from 23.3 to 28.8%, the

strain of the hydrogels exceeded 10 000% strain (Fig. 7b). To further validate the hydrogel's stretchability, a 1 cm hydrogel was stretched to 4.42 m, corresponding to a strain of 42 200% (Fig. 7c). Ji *et al.*¹²⁸ introduced an IL imidazolium salt with a urea backbone (UL) and incorporated sulfobetaine methacrylate (SBMA) and acrylamide (AM) into the hydrogel system (ULAS) through simple one-pot copolymerization. Supramolecular interactions within the IL strengthen the non-covalent bond network of hydrogel-based epidermal electrodes. As the IL concentration increases, the hydrogel exhibits markedly enhanced stress, achieving an elongation at break of 1075% strain and a fracture stress of 343 kPa. Constructing physically crosslinked, entangled, and micelle-crosslinked networks has been demonstrated as an effective way to enhance the mechanical properties of hydrogels. Li *et al.*¹²⁷ prepared a highly stretchable hydrogel with an interpenetrating entangled network by using PAM as the monomer and poly(1-acrylamido-2-methylpropanesulfonic acid) (PAMPS) as the physical crosslinking network, synthesized *via* UV-initiated free radical polymerization (Fig. 7d). The mechanical properties of hydrogels can be tuned by varying the crosslinker concentration. The fracture strain of hydrogels decreases rapidly with increasing crosslinking degree, reaching 4700% strain at a crosslinker content of 1.8 mol% (Fig. 7e). Furthermore, the hydrogel demonstrates outstanding tear resistance.

Hydrogels with a 5 mm pre-cut notch extended to 190 mm and 200 mm under tensile stress without crack propagation. The area of a central circular pre-cut notch expanded approximately 2700-fold during cyclic biaxial stretching (Fig. 7f). Li *et al.*⁵⁴ developed a hydrogel with a multiply crosslinked network by incorporating gelatin and SA into PAM. With the addition of SA, a more complex network structure is formed between PAM/gelatin and SA through hydrogen bonds and electrostatic interactions between molecular chains. As the SA content rises from 0 to 0.8 wt%, the hydrogel's tensile stress increases from 61.3 to 229.3 kPa, with the elongation at break improving from 428.4 to 706.4% strain.

3.4. Gas-permeability

Water vapor and sweat accumulation at the skin–electrode interface can lead to skin irritation and epidermal electrode failure during prolonged monitoring.¹²⁹ Employing gas-permeable conductive hydrogel-based epidermal electrodes has proven an effective solution to this challenge.¹³⁰ Common strategies for enhancing the gas-permeability of conductive hydrogel-based epidermal electrodes include fabricating ultrathin and porous structures.^{129,131} A typical example is that Zhang *et al.*⁴⁹ introduced an ultrathin polyurethane (PU) nanomesh-reinforced gas-permeable hydrogel. The hydrogel was fabricated by immersing the PU nanomeshes in a temperature-sensitive gelatin-based hydrogel solution (Fig. 8a). The resulting ultrathin hydrogel has a thickness of \sim 10.3 μm (Fig. 8b), with excellent mechanical strength (up to 696% strain) and high skin adhesion (area adhesion energy of $176.8 \mu\text{J cm}^{-2}$). Owing to its ultrathin geometry and porous structure, the hydrogel demonstrates a water vapor transmission rate (WVTR) of $1669.3 \pm 23.5 \text{ g m}^{-2} \text{ day}^{-1}$, closely comparable to that of an open bottle ($1742.8 \pm 18.3 \text{ g m}^{-2} \text{ day}^{-1}$) (Fig. 8c).



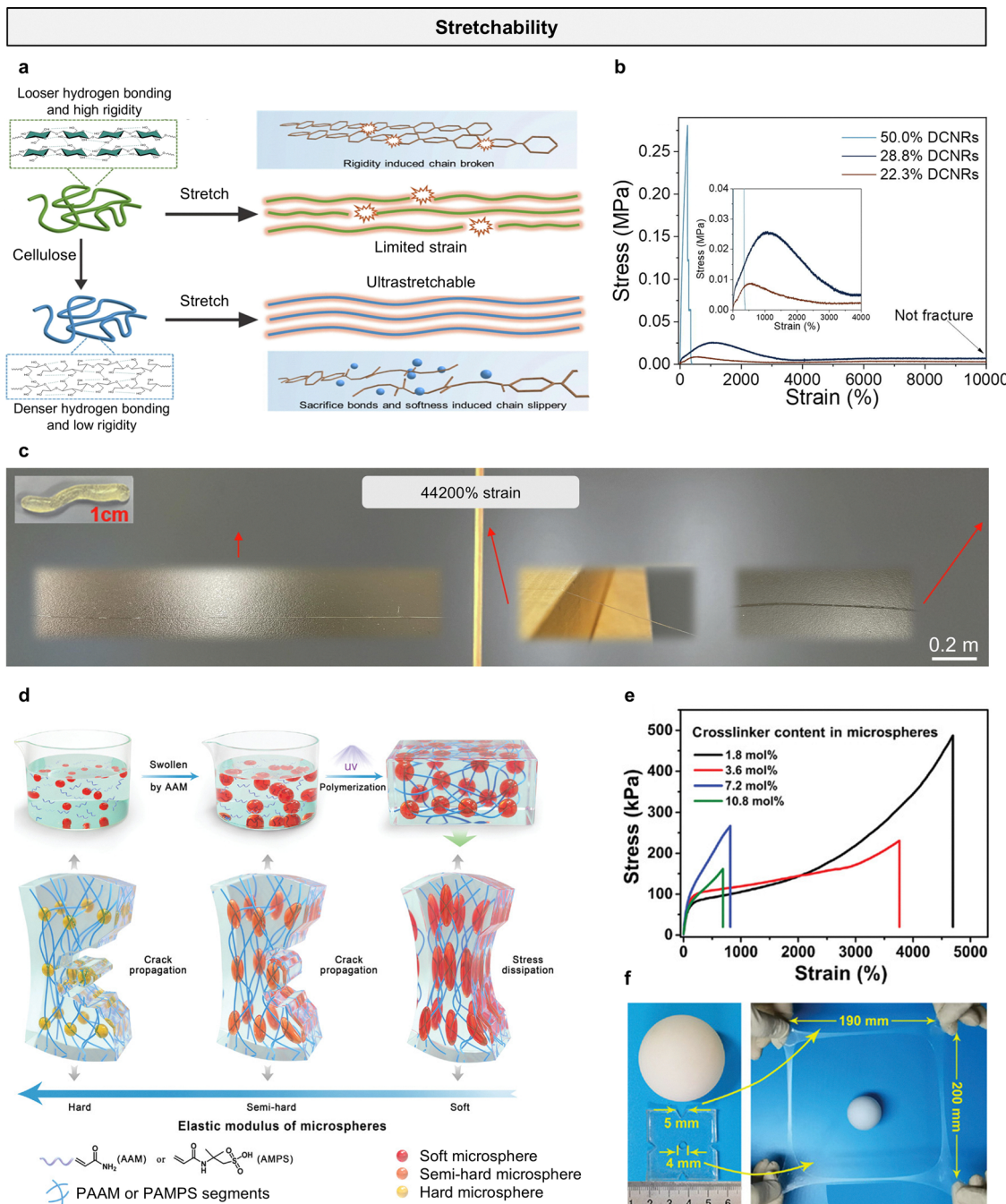


Fig. 7 Stretchability. (a) Schematic illustration of the cleavage of rigid anhydroglucoside unit rings enhances hydrogel chain flexibility and facilitates the reformation of hydrogen bonds during tensile deformation. (b) Stress–strain curves under different DCNRs contents. (c) Photos of DCNRs hydrogel before and after stretching. Reproduced with permission.¹²⁶ Copyright 2024, Wiley-VCH. (d) Schematic illustration of the preparation process and mechanism of super-stretchable hydrogel. (e) Tensile curves of hydrogels under different cross-linker concentrations. (f) Tear resistance of 5 mm long hydrogel under pre-cut equilateral triangle notch. Reproduced with permission.¹²⁷ Copyright 2022, Wiley-VCH.

The resultant ultrathin hydrogel-based epidermal electrode enables long-term, continuous, high-precision electro-physiological monitoring for up to 8 days under everyday conditions.

Cheng *et al.*¹³² developed a cold lamination-based approach to fabricate breathable hydrogel films with precisely controlled thickness and scalability. A mixed solution of PAM and SA is

cast between two polyethylene terephthalate (PET) support films and then rapidly passed through the gap between two rollers. The prepared PET-wrapped hydrogel precursor film is cured under ultraviolet light to complete *in situ* gelation (Fig. 8d). The prepared hydrogel film thickness can be controlled to a minimum of 7 μm . The ultrathin hydrogel film has good skin conformability, and cross-sectional SEM images

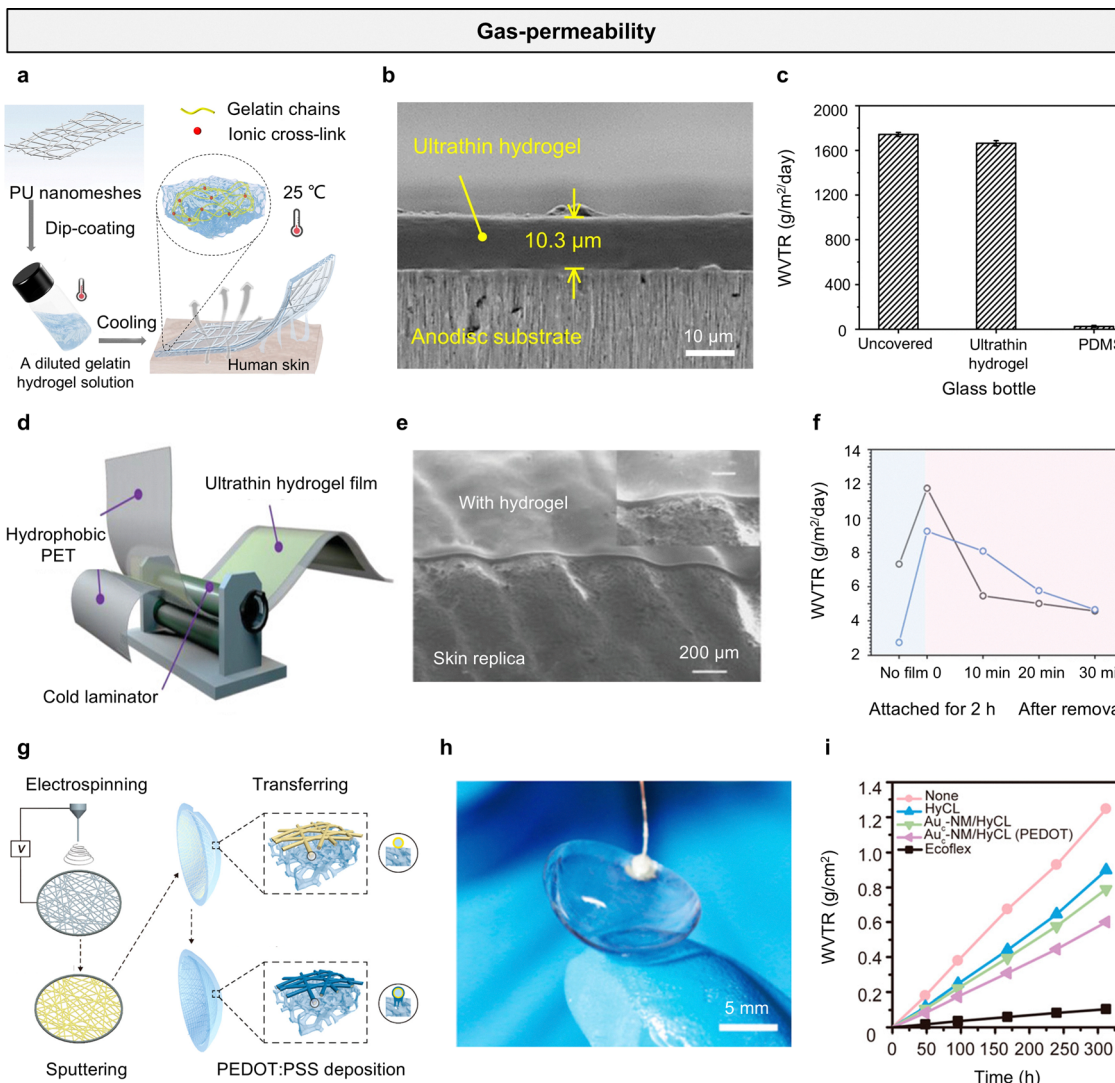


Fig. 8 Gas-permeability. (a) Schematic illustration of the design concept of PU nanomesh-reinforced hydrogels. (b) Cross-sectional SEM image of the ultrathin hydrogel attached on an anodisc substrate. (c) Comparison of WVTR for an uncovered bottle, a bottle covered with 1000-μm-thick PDMS film, and a bottle covered with ~10-μm-thick ultrathin hydrogel, respectively. Reproduced with permission.⁴⁹ Copyright 2024, American Association for the Advancement of Science. (d) Schematic of the cold-lamination method to produce large-area ultrathin hydrogel films. (e) SEM images of a 10 μm thick hydrogel film attached to the fingerprint replica. (f) TEWL and the skin hydration level test by attaching a 3 μm thick parylene film on the forearm of the volunteer. (g) Schematic illustration of the gas-permeable, irritation-free, transparent hydrogel film. Reproduced with permission.¹³² Copyright 2022, Wiley-VCH. (h) Picture of a contact lens-based eye interfacing device based on the hydrogel film. (i) WVTR of open bottle (none), pure hydrogel ocular contact lens (HyCL), HyCL with gold-coated nanofiber mesh (Auc-NM/HyCL), Auc-NM/HyCL with deposition of PEDOT:PSS, and Ecoflex film as a function of elapsed time. Reproduced with permission.¹³³ Copyright 2019, American Chemical Society.

show close contact between a fingerprint replica and a 10 μm thick hydrogel film (Fig. 8e). Due to its ultrathin characteristics, the hydrogel film has good breathability, measured by transepidermal water loss (TEWL). A 50 μm thick hydrogel film and a 3 μm thick impermeable parylene film were attached to the skin, respectively. After applying the ultrathin acrylic film for 2 hours, the initial skin hydration level increased from approximately 25 to 45%. Accompanying this, the TEWL significantly increased from ~7 to 12 g m⁻² day⁻¹. After removing the acrylic film, the skin moisture level dropped to ~28% within 30 minutes, and the TEWL also decreased (Fig. 8f).

Wei *et al.*¹³³ reported a breathable, non-irritative, and transparent hydrogel film. The gas-permeable film was fabricated using a metal-coated nanofiber network (metal_c-NM) as the electronic conductor and a commercial hydrogel contact lens as the substrate, with *in situ* electrochemical deposition of PEDOT:PSS employing the metal_c-NM as the electrode (Fig. 8g). The resultant hydrogel film exhibits an optical transparency of 90% (Fig. 8h). Owing to the highly porous structure of the metal_c-NM film, the underlying hydrogel substrate retains its breathability, enabling the hydrogel film to demonstrate excellent breathability with a WVTR of approximately 69.2 mg cm⁻² day⁻¹,

significantly exceeding that of an impermeable Ecoflex film at $7.98 \text{ mg cm}^{-2} \text{ day}^{-1}$ (Fig. 8i).

4. Applications of conductive hydrogel-based epidermal electrodes in electrophysiological monitoring

Conductive hydrogel-based epidermal electrodes, due to their good conductivity, outstanding skin adhesion and compliance, excellent stretchability, and superior breathability, have shown great potential in the field of electrophysiological signal monitoring. In this section, we will summarize the representative progress of conductive hydrogel-based epidermal electrodes in ECG, EMG, EEG, and EOG monitoring.

4.1. Electrocardiogram monitoring

ECG signals play a pivotal role in the medical field, being extensively utilized for diagnosing cardiovascular diseases,^{134–137} and assessing cardiac health.^{138–140} Conductive hydrogel-based epidermal electrodes possess distinctive properties, including high conductivity, excellent stretchability, and strong interfacial adhesion.^{141,142} These attributes enable them to achieve superior SNR and sensitivity compared to traditional rigid electrodes, thereby enhancing the accuracy and reliability of monitoring and providing more precise data to support clinical diagnostics and treatment.

A typical example is that Yang *et al.*¹⁴³ developed a wireless Nepenthes-inspired hydrogel (NIH) hybrid system. The hybrid system consists of a skin electrode assembled from a flexible circuit module, an electrode connector with a hollow structure, a stretchable silicone joint, and three Nepenthes-inspired hydrogel interface layers (Fig. 9a). The DN hydrogel based on PVA/PAA enhances its adhesion to the skin (3.9 kPa). To evaluate the practicality of the NIH hydrogel system during motion, the system was laminated on the skin above the subject's heart to collect ECG signals (Fig. 9b). To evaluate the stability of the NIH system, heart rate curves were recorded using the system and a commercial device (*i.e.*, Polar H10 heart rate strap) under motion conditions, respectively. The results demonstrate that data from both systems reveal nearly identical heart rate variation trends, with a relative deviation of less than 2.6% over 5 minutes, validating the accuracy of the NIH system (Fig. 9c).

Inspired by the pentaradial symmetry of starfish, Chen *et al.*¹⁴⁴ introduced a starfish-like wearable hydrogel-based bioelectronic system for high-fidelity ECG monitoring. The skin interface layer consists of conductive hydrogels for five sensing pads and non-conductive hydrogels for the central hub, while the serpentine arms remain independent. The device is constructed on a 25 μm -thick polyimide (PI) substrate, utilizing copper traces as conductive pathways. Its pentaradial design incorporates five serpentine arms, each equipped with an independent sensing element at its tip, all linked to a central electronic hub for data processing and wireless transmission. Signals are processed by a 32-bit microcontroller and transmitted wirelessly, with analyzed data presented intuitively on a

mobile device (Fig. 9d). By employing a conductive adhesive hydrogel as the electrode–skin interface and a mechanically decoupled starfish-inspired device design (Fig. 9e), this device enables high-fidelity ECG recordings across diverse motion states, sustaining an SNR of approximately 35 dB even during running. The system enables real-time, high-precision diagnosis of cardiac conditions by integrating ECG, seismocardiogram, and gyrocardiogram signals with a deep learning model, achieving classification accuracies of 91.31% for normal conditions, 94.03% for atrial fibrillation, 91.67% for myocardial infarction, and 91.66% for heart failure. Fig. 9f shows the cardiac mechanical and electrical biosignals captured by a hydrogel-based device during walking in a patient clinically diagnosed with heart failure. The signals show reduced Q and T peaks, irregular heart rate, interrupted electromechanical delay, and altered pre-ejection period/left ventricular ejection time parameters, indicating electrophysiological disturbances. Additionally, the patient's cardiac mechanical activity is significantly impaired, with a contraction amplitude nearly 60% lower than that of healthy individuals (Fig. 9g). These results demonstrate the ability of hydrogel-based epidermal electrodes to achieve high-fidelity recording of cardiac signals.

4.2. Electromyography monitoring

EMG is a technique for recording electrophysiological activity associated with muscle contraction and relaxation.¹⁴⁵ As EMG signals directly reflect neuromuscular activity, they are extensively utilized in human motion monitoring,^{146–148} controlling human-machine interfaces,^{149–151} and diagnosing neuromuscular disorders.^{45,152,153} However, the impedance between the electrode and skin affects the quality of EMG signals in practical applications, so researchers have increasingly focused on enhancing the conductivity and skin adhesion of hydrogel-based epidermal electrodes to achieve low interface impedance.^{142,154–157} For instance, Tian *et al.*¹⁵⁸ leveraged the liquid-to-solid transition concept to develop an *in situ* hydrogel-based epidermal electrode for monitoring post-fatigue muscle recovery (Fig. 10a). To develop a hydrogel with rapid *in situ* gelation, a formulation of gelatin, PEDOT:PSS, and a deep eutectic solvent (DES) was employed. At temperatures above 60 °C, gelatin exists as individual molecular chains. Upon cooling, the gelatin network solidifies *via* hydrogen bonding and physical crosslinking, with PEDOT:PSS forming a conductive network within the gelatin matrix (Fig. 10b). DES demonstrate superior thermal stability and ionic conductivity. The hydroxyl groups in DES engage with the polymer network *via* hydrogen bonding and ionic interactions, improving solubility, stability, and network formation. The *in situ*-formed hydrogel exhibits exceptional adhesion (591 kPa) and minimal skin contact impedance (10.2 kΩ). The prepared *in situ* biogel epidermal electrode was used to monitor muscle recovery after exercise-induced fatigue. EMG signals from the left and right calves were recorded when volunteers performed toe-raising exercises (Fig. 10c). After prolonged exercise (running for 45 minutes), the hydrogel epidermal electrode recorded EMG signals at different stages, with an SNR of up to 30 dB (Fig. 10d). Hydrogel-based epidermal electrodes were employed to monitor muscle



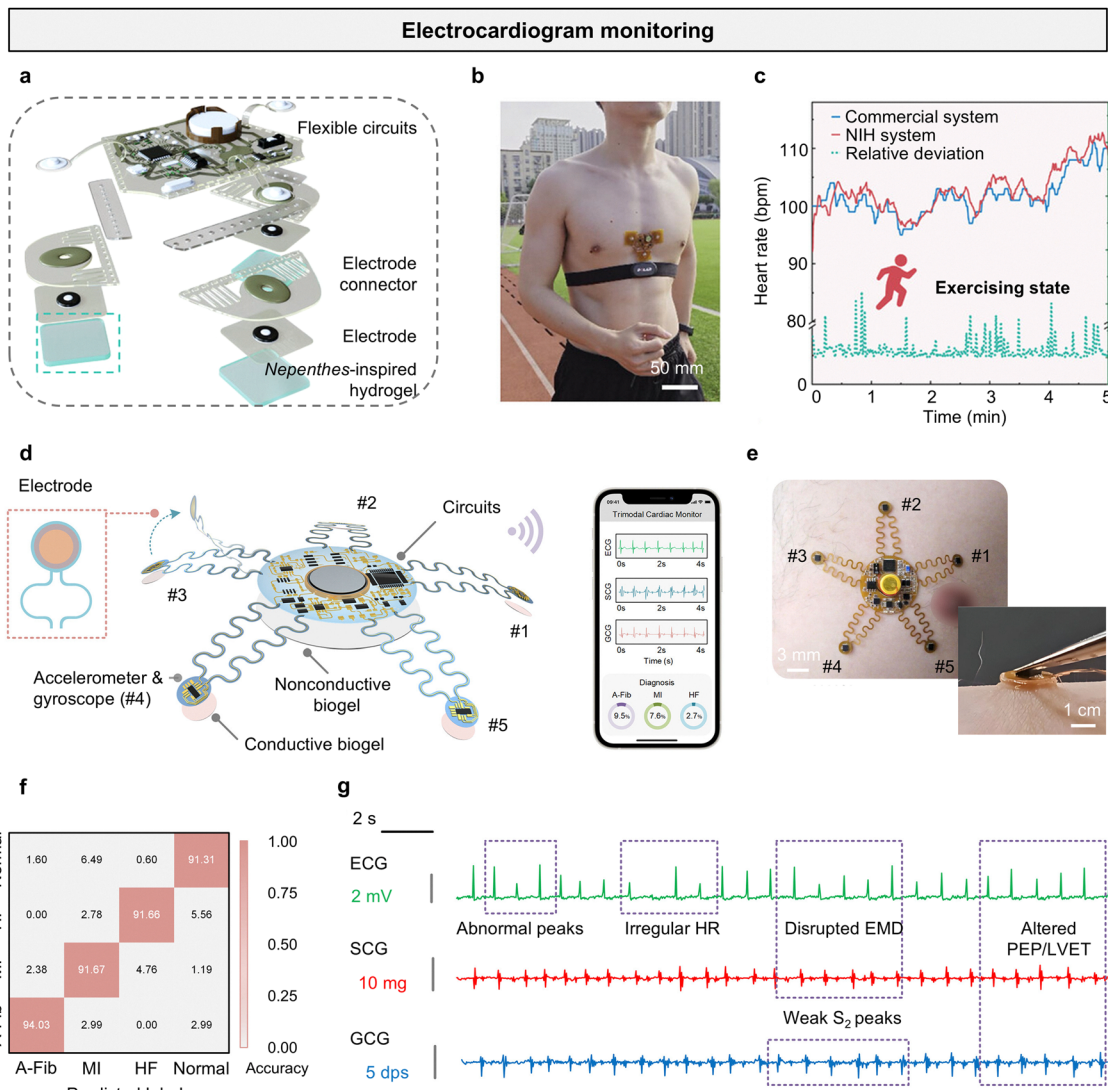


Fig. 9 Electrocardiogram monitoring. (a) Exploded 3D model of the NIH hybrid system. (b and c) Heart rate and relative deviation curves measured by the NIH system and commercial system under the subject's exercising states. Reproduced with permission.¹⁴³ Copyright 2024, Wiley-VCH. (d) Schematic illustration of the starfish-like device for trimodal cardiac monitoring during motion. (e) Optical image showing the device applied to the chest skin, with the five strategically positioned sensing pads, and optical image, showing robust adhesion of the sensing pad to human skin, facilitated by the conductive hydrogels. The image features a tweezer used to stretch the sensing pad from the skin. (f) Confusion matrix, demonstrating the classification accuracy for predicting each type of heart disease and normal signals in the test set. During use, the starfish-like device can display the real-time classification probabilities on smart devices. (g) Cardiac electrical and mechanical signals collected by the starfish-like wearable device from a HF patient during walking; dps, degrees per second. Reproduced with permission.¹⁴⁴ Copyright 2025, American Association for the Advancement of Science.

signals in volunteers during extended sedentary periods, revealing a decline in average muscle frequency over time. After 24 hours, the mean muscle frequency started to rise, approaching pre-exercise levels by 48 hours, signifying full recovery from exercise-induced fatigue. To quantitatively assess muscle fatigue recovery, the recovery percentage was defined as the ratio of mean EMG frequencies before and after exercise-induced fatigue. This recovery metric enables precise evaluation of muscle condition, supporting exercise and recovery planning, as well as monitoring recovery from muscle-related disorders. Liu *et al.*⁹⁹ designed high-performance hydrogel-based epidermal electrodes by incorporating numerous interpenetrating core-sheath con-

ductive nanofibers into a physically crosslinked polyelectrolyte network. The hydrogel is composed of cellulose nanofibers, PAA, and PEDOT:PSS (Fig. 10e). The hydrogel-based epidermal electrode was fabricated as a $10 \times 10 \text{ cm}^2$ multi-pixel skin array, showcasing its capability to capture human motion across various postures (Fig. 10f). As an interface for human-machine interaction, the hydrogel epidermal electrode exhibits good interfacial adhesion (adhesion energy of 28 kPa on pig skin) and a low electrochemical impedance of 42Ω . Fig. 10g shows that after peeling from the skin, a typical "fibrillation" phenomenon occurs, confirming effective adhesion between the hydrogel epidermal electrode and the skin (Fig. 10h). To evaluate the

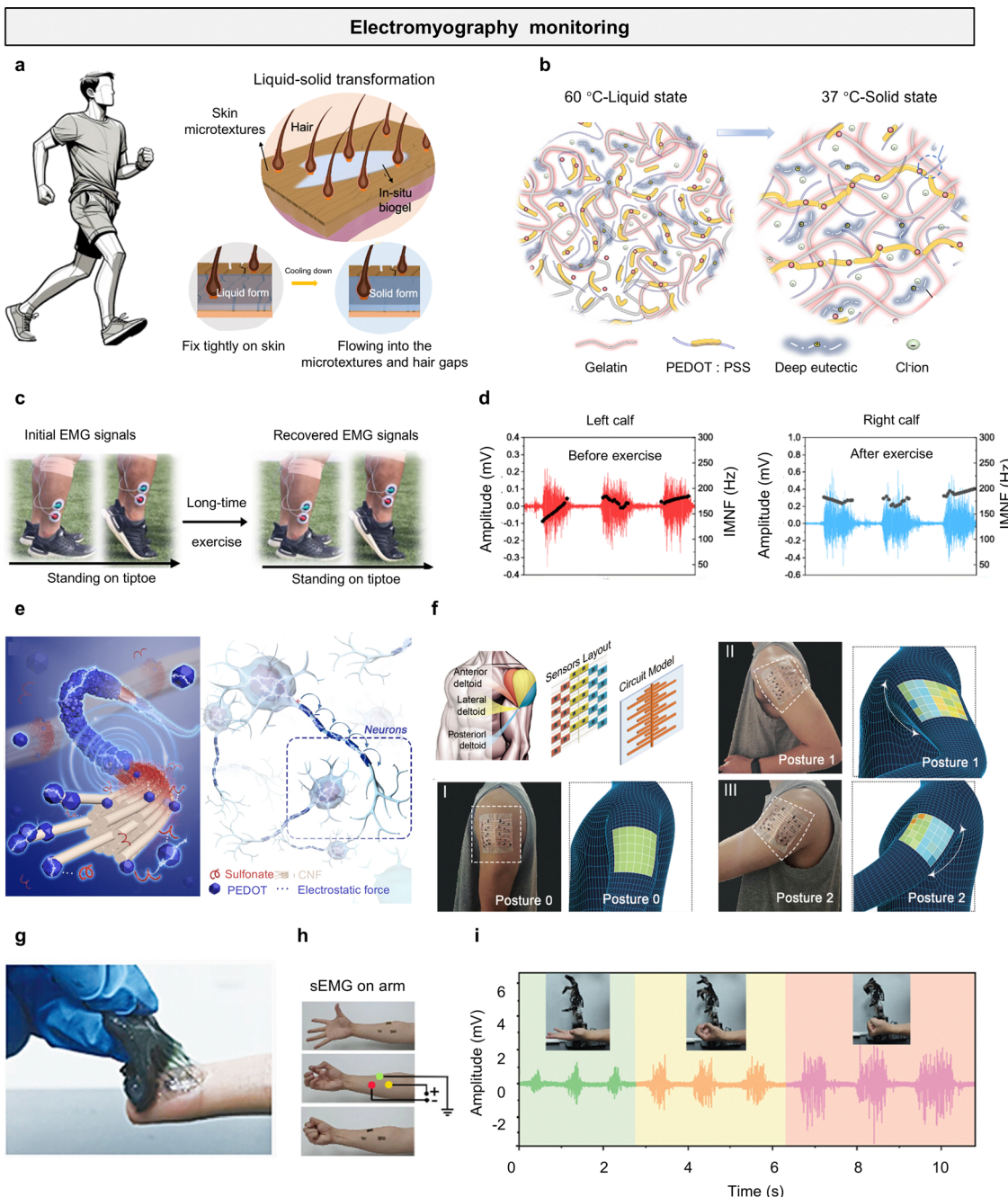


Fig. 10 Electromyography monitoring. (a) Liquid-to-solid transformation concept and the application of *in situ* biogel. (b) Schematic diagram and optical images of the *in situ* rapid gelation process of the biogel. (c) Procedure for recovery monitoring using *in situ* biogel. Comparison of initial EMG signals with those after fatigue. (d) Initial EMG signals and post-exercise signals for left and right calves. Reproduced with permission.¹⁵⁸ Copyright 2025, Nature Publishing Group. (e) Schematic illustration of the biomimetic segmentally conductive fiber hydrogel. (f) Sensor array layout and circuit model designed for monitoring muscle movements. (g) Photograph of the self-adhesive hydrogel after peeling. (h and i) EMG signals on the forearm at different grip force levels. Reproduced with permission.⁹⁹ Copyright 2024, American Chemical Society.

human-machine interaction capability of the hydrogel epidermal electrode, the electrode was used to test EMG signals on the forearm under different grip strength levels, and the recorded arm EMG signals could be customized to precisely control a prosthetic limb, thereby achieving various robotic gestures with adjustable grasping angles and force levels (Fig. 10i).

4.3. Electroencephalogram monitoring

EEG is an electrophysiological monitoring method for recording brain electrical activity.¹⁵⁹ It mainly originates from post-synaptic potentials and has significant application potential in sleep monitoring,^{160–162} emotion recognition,^{163–165} and brain-computer interfaces.^{166–168} The presence of scalp hair and the



head's intricate, curved contours pose significant challenges in achieving stable and effective contact between epidermal electrodes and the scalp for prolonged EEG recordings.¹⁶⁹ To overcome this challenge, Wang *et al.*¹⁷⁰ developed a conductive gel-based epidermal electrode for skin application, featuring a temperature-responsive reversible liquid-to-gel transition. This phase transition endows the hydrogel with unique skin coating

and *in situ* gelation properties (Fig. 11a). The fluidity of the conductive hydrogel enables good compliance and conformal contact with hairy scalps without hair interference, surpassing prefabricated gels, which facilitates high-quality EEG recording through hairy scalps (Fig. 11b). The conductive hydrogel-based epidermal electrode was utilized to capture EEG signals during open-eye and closed-eye conditions, revealing distinct

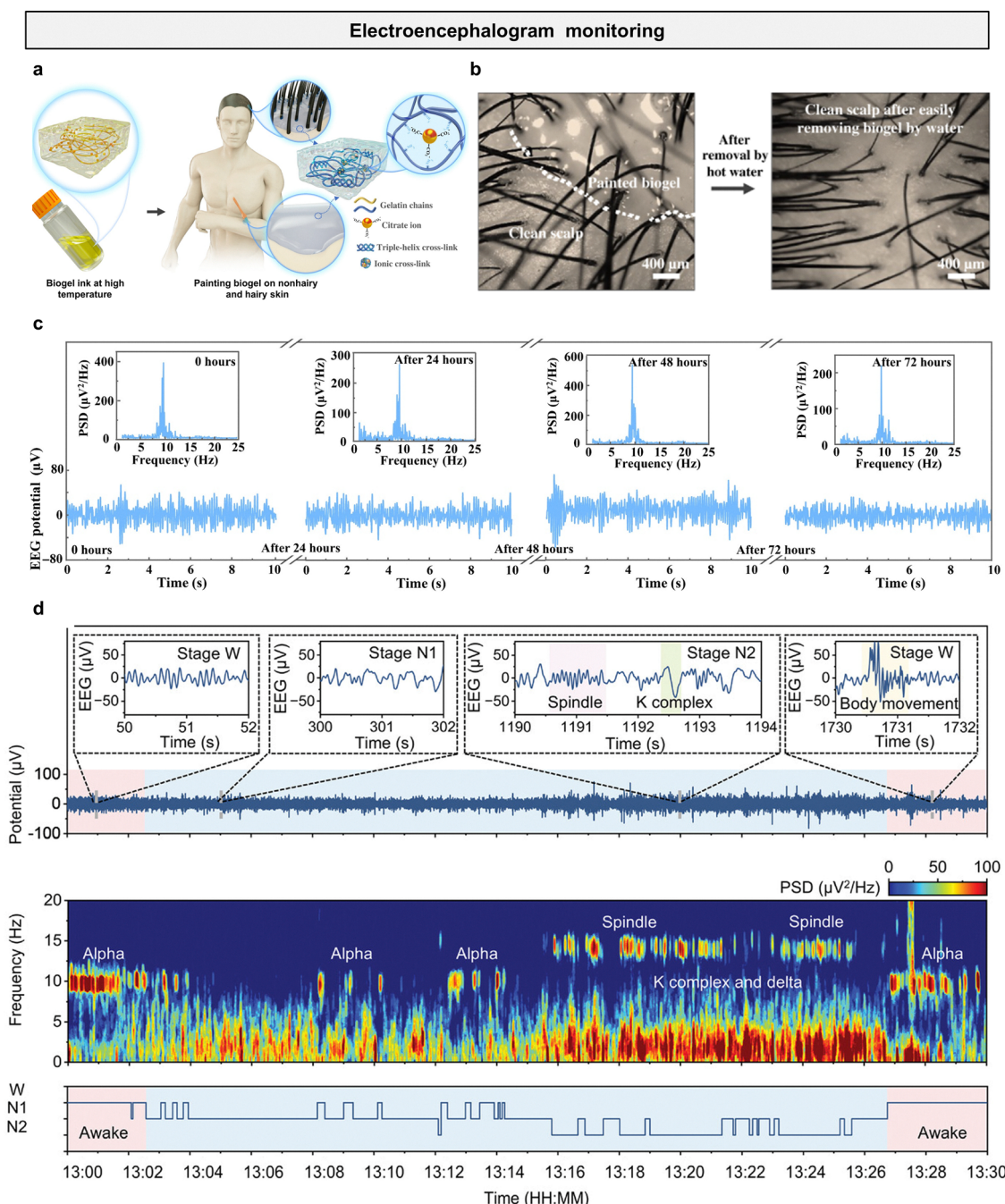


Fig. 11 Electroencephalogram monitoring. (a) Schematic illustration showing the concept of on-skin paintable biogel for hairy scalp for EEG recording. (b) Optical images of biogel painted on the hairy scalp and clean scalp after removing biogel by water. (c) EEG alpha rhythms recorded by the painted biogel electrode after continuous wearing for 0, 24, 48, and 72 hours. Reproduced with permission.¹⁷⁰ Copyright 2022, American Association for the Advancement of Science. (d) Continuous wireless monitoring of EEG signals using paintable Gel-GGGLiCit hydrogels and the multitaper spectrogram of the EEG signals (top) and visually scored hypnogram (bottom). Reproduced with permission.¹⁷¹ Copyright 2024, Wiley-VCH.

differences between the signals in these paradigms. Due to its relatively long-term electrical stability, excellent mechanical interaction (73.4 ± 2.2 kPa), and stable contact with the scalp (6.95 ± 0.97 k Ω), the conductive hydrogel epidermal electrode recorded α signals with no significant differences across different wearing durations (0, 24, 48, and 72 hours), with high quality and a peak frequency of 10 Hz (Fig. 11c). This indicates that the applicable conductive hydrogel epidermal electrode has promising capabilities for long-term high-fidelity EEG recording. To enable continuous high-fidelity EEG signal detection, paintable hydrogel-based epidermal electrodes require a streamlined and rapid gelation process to minimize adhesion-related damage from slow gelation and reduce subject discomfort. Li *et al.*¹⁷¹ developed a paintable, fast-gelling, and highly adhesive hydrogel-based epidermal electrode *via* a one-pot synthesis. Comprising gelatin, gallic acid, sodium citrate, LiCl, glycerol, and Tris-HCl buffer (Gel-GGLiCit), the hydrogel possesses reversible thermal phase transition properties, facilitating skin compatibility and rapid *in situ* gelation within 15 seconds. Furthermore, the paintable hydrogel-based epidermal electrode can form a conformal interface with hairy scalps (3.36 mJ cm^{-2}) in its fluid state prior to gelation, allowing it to penetrate dense hair effectively. These properties substantially lower scalp contact impedance, with the electrode achieving a reduced skin contact impedance of 45.64 k Ω compared to 62.70 k Ω for commercial pastes. To assess the potential of the paintable hydrogel-based epidermal electrode for sleep stage monitoring and sleep disorder analysis, it was employed to capture EEG signals from subjects during brief daytime naps. In addition to the awake state, the subject's 30-minute sleep primarily involved non-rapid eye movement (NREM) sleep, stages N1 and N2. Stage N1 marks the initial phase of sleep, defined by the transition from wakefulness to sleep, where individuals experience light sleep and are easily roused. Following N1, stage N2 emerges as a deeper sleep phase, characterized by a reduced heart rate and the occurrence of sleep spindles (Fig. 11d). During the awake stage (W), elevated power in the alpha band (8–12 Hz) is evident in EEG signals, most pronounced during eye closure. As wakefulness transitions to stage N1, alpha band power progressively diminishes and eventually disappears. These findings demonstrate that high-fidelity raw EEG data, acquired with paintable hydrogel-based epidermal electrodes, enable clear visualization of critical EEG features throughout sleep.

4.4. Electrooculography monitoring

EOG is a technique that measures eye movement and position by recording electrical potentials around the eyes, widely used for diagnosing ophthalmic and neurological disorders,^{172,173} supporting human-computer interaction,^{174,175} studying cognitive processes,^{176,177} and assessing fatigue and alertness.^{178,179} Zheng *et al.*¹⁸⁰ developed a thermoresponsive gelatin-based hydrogel (GGW) *via* a one-pot synthesis, incorporating glycerol, ammonium chloride (NH₄Cl), and water (Fig. 12a). The *in situ*-formed hydrogel electrode demonstrates robust adhesion at the hydrogel-skin interface (0.9 N cm^{-1}), enabling conformal skin contact and high-fidelity signal acquisition (Fig. 12b).

The hydrogel was placed around the eyes for EOG signal monitoring, and then the signals were transmitted through a Bluetooth-enabled portable wireless module for real-time data collection. Fig. 12c illustrates representative EOG signals acquired with hydrogel-based epidermal electrodes, exhibiting pronounced periodic waveforms as the subject repeatedly shifts their gaze from side to side. Notably, the EOG signals obtained using the hydrogel epidermal electrode exhibit higher amplitude than those recorded using commercial paste. Meanwhile, the SNR (21.2 dB) of the hydrogel epidermal electrode surpasses that of the commercial paste (20.5 dB) (Fig. 12d).

To validate the capability of the hydrogel epidermal electrode in acquiring EOG signals from patients with speech impairments, Pan *et al.* reported a multifunctional PAA hydrogel catalyzed by oxidative metal-ion-free lignin.¹⁸¹ By incorporating transition metal ions and sodium lignosulfonate (LS), LS rapidly reduces Fe³⁺ to Fe²⁺, thereby promoting the rapid generation of free radicals by APS (initiator) at room temperature. This mechanism accelerates the polymerization of vinyl monomers, enabling the rapid assembly of the hydrogel (Fig. 12e). The hydrogel exhibits excellent flexibility (~ 7 kPa), remarkable stretchability ($\sim 2700\%$ strain), and strong skin adhesion (~ 9 kPa).

Notably, the hydrogel, integrating these superior properties, can serve as an epidermal electrode for the human body, offering a viable alternative to conventional commercial electrodes. Fig. 12f illustrates a volunteer wearing the PAA-LS-0.05 hydrogel epidermal electrode undergoing an EOG test. The volunteer simulated a patient with severe physical and verbal impairments, retaining only limited facial skin mobility and lacking the ability to speak or type. To address this, the actions of closing the left and right eyes were defined as “+” and “−”, respectively (Fig. 12g), and a reference table comprising 26 English letters and punctuation marks was developed. Through regular eye movements, the patient could achieve linguistic output and communication. As shown in Fig. 12h, the patient successfully produced the unordered sequence “FAFU” *via* eye movements, with the signal being clearly readable. Subsequently, the patient further expressed the English word “THANKS” (Fig. 12i) and the French word “MERCI” (meaning “thank you”, Fig. 12j) through eye movements. This wearable hydrogel electrode seamlessly integrates with the eye-movement-based communication system, offering a significant and urgent solution to address communication challenges for such patients.

While conductive hydrogel-based epidermal electrodes have demonstrated excellent performance across various electrophysiological modalities—including ECG, EMG, EEG, and EOG—their practical deployment in dynamic, real-world environments poses additional challenges related to signal stability and quality. Motion artifacts remain a major concern in wearable and long-term bioelectronic monitoring, often arising from skin deformation, electrode displacement, or body movement. These artifacts can significantly distort low-amplitude biopotentials—particularly in EEG and ECG recordings—thereby compromising signal fidelity and diagnostic accuracy. The intrinsic softness, stretchability, and conformability of hydrogel-based electrodes help maintain stable skin-electrode contact, effectively minimizing impedance



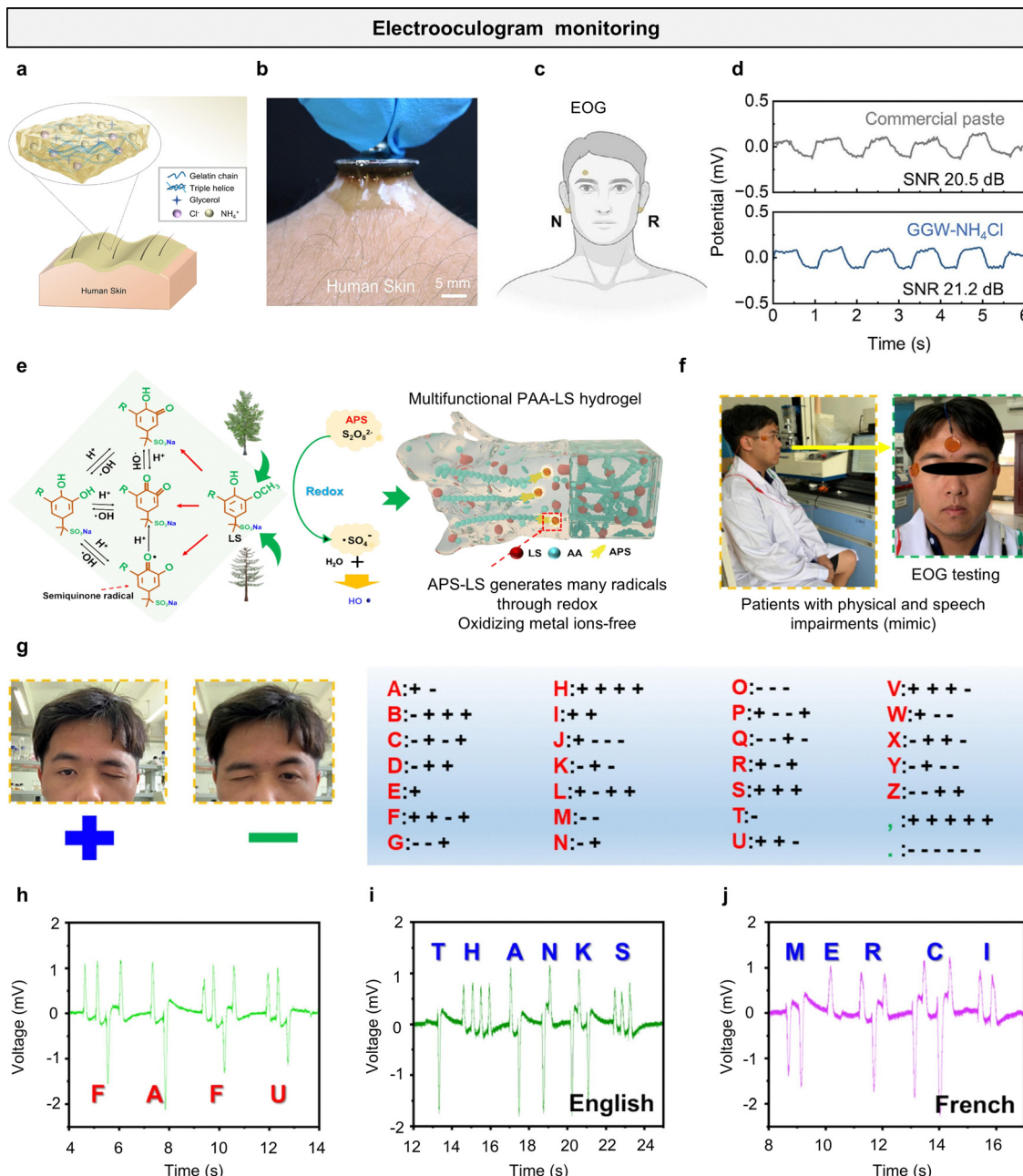


Fig. 12 Electrooculography monitoring. (a) Schematic view depicting the concept of a skin-printable hydrogel. (b) Photograph showing the attachment of Ag/AgCl electrode to the GGW-NH₄Cl hydrogel, highlighting the superior adhesion. (c) Schematic of electrode positions for EOG signal measurements. (d) EOG signals recorded using commercial paste (top) and the GGW-NH₄Cl hydrogel (bottom), along with the corresponding SNR. Reproduced with permission.¹⁸⁰ Copyright 2025, Elsevier. (e) Schematic illustration of the preparation, function, and application of oxidative metal ions-free lignin-catalyzed hydrogels. (f) Schematic diagram of PAA-LS-0.05 hydrogel-based bioelectrodes adhered to the skin of a volunteer's head for EOG monitoring. (g) Schematic diagram of the codable eye communication mechanism. (h) The gel electrodes detected the volunteers' eye movements, which the device interpreted as the word "FAFU". This volunteer effectively produced the outputs (i) "thanks" and (j) "merci" (French). Reproduced with permission.¹⁸¹ Copyright 2025, Elsevier.

fluctuations and suppressing artifact generation at the source. Additionally, signal processing techniques such as adaptive filtering, baseline drift correction, and motion-sensor-assisted denoising are widely employed to further improve signal quality. Therefore, the integration of material-level optimization and algorithmic post-processing is essential for achieving reliable, high-fidelity electrophysiological recordings under real-life conditions.

5. Summary and perspectives

Conductive hydrogels, characterized by their intrinsic flexibility, tunable properties on adhesion and electrical conductivity, hold significant promise for the development of high-performance epidermal electrodes. This review offers a comprehensive overview of recent advances in conductive hydrogel-

based electrodes for electrophysiological monitoring. We first examined the underlying conductive mechanisms—ionic, electronic, and hybrid pathways—followed by a discussion of the essential properties required for effective signal acquisition, such as high conductivity, strong adhesion, stretchability, and breathability. Finally, we highlighted recent progress in their application across various electrophysiological monitoring scenarios. Despite notable achievements, several challenges persist that must be addressed to fully realize their potential.

5.1. Advancements in materials and conductivity mechanisms

The future development of conductive hydrogel-based epidermal electrodes will be driven by innovations in materials science and the continued refinement of conductivity mechanisms. While current strategies largely focus on ionic, electronic, and hybrid conduction, future research will likely prioritize optimizing these mechanisms for enhanced signal fidelity and long-term stability. Incorporating advanced conductive polymers and nanomaterials could significantly improve electronic conductivity, overcoming the environmental sensitivity associated with ionic pathways. Additionally, bioinspired designs—such as the integration of conductive peptides or materials that mimic the skin's natural electrical properties—offer the potential for improved biocompatibility and seamless integration with biological systems. These innovations aim to produce electrodes capable of reliable, high-quality electrophysiological monitoring in dynamic and diverse conditions.

5.2. Strategies for long-term reliability

Long-term performance and durability of conductive hydrogel-based epidermal electrodes can be greatly enhanced through advanced materials design and interfacial engineering. One promising direction is the development of fatigue-resistant architectures, such as self-healing polymer networks and dynamic crosslinking systems, which can maintain mechanical integrity under repeated deformation. Hybrid structures that combine elastomers with hydrogels may further improve stretchability and resistance to cracking. To address adhesion challenges under real-world conditions—such as perspiration, oily skin, or continuous body motion—bioinspired adhesive strategies present an exciting pathway. These may include catechol-functionalized chemistries, microstructured surface designs, or reversible covalent bonding, enabling robust and repeatable skin contact. Advances in hydration management are also expected to play a crucial role in maintaining performance over extended use. Future studies may explore the integration of moisture-retentive additives, breathable yet protective encapsulation materials, or systems capable of autonomous hydration regulation to prevent dehydration and ion leaching.

5.3. Multifunctionality and smart features

Beyond signal monitoring, the next generation of conductive hydrogel electrodes is expected to embrace multifunctionality and smart responsiveness. One promising direction is the development of closed-loop systems, where electrodes not only

detect physiological signals but also trigger therapeutic interventions, such as on-demand drug delivery. Incorporating self-healing capabilities through dynamic covalent bonds or supramolecular interactions could greatly enhance durability, especially under mechanical strain during long-term use. Additional smart features—such as energy harvesting from body movement or adaptive behavior in response to skin conditions—could further extend the functionality and lifespan of these devices. These advancements will transform conductive hydrogels into versatile, intelligent platforms that bridge sensing, therapy, and human-machine interfaces.

5.4. Wearability, data integration, and personalized medicine

The long-term vision for conductive hydrogel-based epidermal electrodes lies in their seamless integration into wearable systems that support comfort, continuous data acquisition, and personalized healthcare. Innovations in material design—particularly ultrathin, breathable, and skin-conformal hydrogels—will be crucial to improving wearability and minimizing skin irritation during extended use. Simultaneously, integrating these devices with advanced data analytics and machine learning algorithms will unlock their potential for real-time monitoring, predictive diagnostics, and personalized treatment strategies. This convergence of soft materials, digital health, and precision medicine heralds a shift toward proactive, patient-centered care, where electrophysiological monitoring becomes not just reactive but a key driver in managing health and disease.

Author contributions

Jiawei Yang: writing – origin draft, writing – review & editing, investigation, data curation. Yi Liu: writing – origin draft, writing – review & editing, resources, methodology, data curation. Wenqing Yan: writing – review & editing, formal analysis. Pengcheng Zhou: writing – review & editing, formal analysis. Zonglei Wang: writing – review & editing, formal analysis. Yuli Wang: writing – review & editing. Yujie Zhang: writing – review & editing, formal analysis. Zongman Zhang: writing – review & editing, software. Fan Mo: writing – review & editing. Zichong Ji: writing – review & editing. Hossam Haick: writing – review & editing. Yan Wang: writing – review & editing, project administration, funding acquisition, conceptualization.

Conflicts of interest

The authors declare that they have no known competing financial interests or personal relationships that could have appeared to influence the work reported in this paper.

Data availability

No primary research results, software or code have been included and no new data were generated or analysed as part of this review.



Acknowledgements

The authors sincerely acknowledge the support from the Natural Science Foundation of China (grant no. 52303371, W2521021), Guangdong Science and Technology Department (grant no. STKJ2023075, 2022A1515110209, 2021B0301030005), seed fund from GTIIT Changzhou Innovation Institute (grant no. GCII-Seed-202406), and the Key Discipline (KD) Fund, the Technion, and the Start-Up Fund from Guangdong Technion.

Notes and references

- Y. Xiang, K. Shi, Y. Li, J. Xue, Z. Tong, H. Li, Z. Li, C. Teng, J. Fang and N. Hu, *Nano-Micro Lett.*, 2024, **16**, 132.
- J. P. Piccini, A. M. Russo, P. S. Sharma, J. Kron, W. Tzou, W. Sauer, D. S. Park, U. Birgersdotter-Green, D. S. Frankel and J. S. Healey, *Circ.: Arrhythmia Electrophysiol.*, 2022, **15**, e009911.
- K. E. Odening, A.-M. Gomez, D. Dobrev, L. Fabritz, F. R. Heinzel, M. E. Mangoni, C. E. Molina, L. Sacconi, G. Smith and M. Stengl, *EP Europace*, 2021, **23**, 1795–1814.
- A. H. Caillet, A. T. Phillips, L. Modenese and D. Farina, *J. Electromyogr. Kinesiol.*, 2024, **76**, 102873.
- R. Sun, A. Sohrabpour, G. A. Worrell and B. He, *Proc. Natl. Acad. Sci. U. S. A.*, 2022, **119**, e2201128119.
- F. Arcuri, C. Porcaro, I. Ciancarelli, P. Tonin and A. Ceresa, *Electronics*, 2021, **10**, 836.
- M. Pyasik, M. Scandola and V. Moro, *Neuropsychologia*, 2022, **174**, 108333.
- CTRL-labs at Reality Labs, D. Sussillo, P. Kaifosh and T. Reardon, *bioRxiv*, 2024, preprint, 2024.02.23.581779, DOI: [10.1101/2024.02.23.581779](https://doi.org/10.1101/2024.02.23.581779).
- H. Zhang, D. Zhang, Z. Wang, G. Xi, R. Mao, Y. Ma, D. Wang, M. Tang, Z. Xu and H. Luan, *ACS Appl. Mater. Interfaces*, 2023, **15**, 5128–5138.
- J. W. Kam, T. Rahnuma, Y. Park and C. Hart, *NeuroImage*, 2022, **258**, 119372.
- M. Zhu, H. Wang, S. Li, X. Liang, M. Zhang, X. Dai and Y. Zhang, *Adv. Healthcare Mater.*, 2021, **10**, 2100646.
- Y. Luo, W. Li, Q. Lin, F. Zhang, K. He, D. Yang, X. J. Loh and X. Chen, *Adv. Mater.*, 2021, **33**, 2007848.
- P. Kateb, J. Fan, J. Kim, X. Zhou, G. A. Lodygensky and F. Cicoira, *Flexible Printed Electron.*, 2023, **8**, 045006.
- J. Kim, J. Fan, G. Petrossian, X. Zhou, P. Kateb, N. Gagnon-Lafrenais and F. Cicoira, *Mater. Horiz.*, 2024, **11**, 3548–3560.
- X. Zhou, P. Kateb, J. Fan, J. Kim, G. A. Lodygensky, B. Amilhon, D. Pasini and F. Cicoira, *J. Mater. Chem. C*, 2024, **12**, 5708–5717.
- F. Han, X. Huang and E. Teye, *J. Food Process. Eng.*, 2019, **42**, e12983.
- Q. Ouyang, Y. Yang, J. Wu, Q. Chen, Z. Guo and H. Li, *LWT*, 2020, **118**, 108768.
- W. Zhang, C. Liu, F. Liu, X. Zou, Y. Xu and X. Xu, *Food Chem.*, 2020, **303**, 125378.
- B. Lu, F. Han, J. H. Aheto, M. M. Rashed and Z. Pan, *Food Sci. Nutr.*, 2021, **9**, 5220–5228.
- H. Yin, X. Hu, X. Huang, X. Zou, Y. Xu, J. Shi and M. Yang, *Food Anal. Methods*, 2021, **14**, 1836–1842.
- S. Yang and X. Jiang, *ACS Nano*, 2024, **18**, 27107–27125.
- H. Ullah, M. A. Wahab, G. Will, M. R. Karim, T. Pan, M. Gao, D. Lai, Y. Lin and M. H. Miraz, *Biosensors*, 2022, **12**, 630.
- J. Yi, Y. Gu, J. Yang, Z. Wang, Y. Wang, W. Yan, Q. Sun, P. Zhou, Y. Xu, X. He, J. Zhong and Y. Wang, *Mater. Horiz.*, 2025, **12**, 4714–4723.
- J. Yang, Q. Sun, Z. Wang, Y. Xu, Y. Wang, W. Yan, P. Zhou, Z. Ji, H. Jiang, S. Chen, W. Zhang, H. Haick and Y. Wang, *Wearable Electron.*, 2025, **2**, 55–61.
- H. Wu, G. Yang, K. Zhu, S. Liu, W. Guo, Z. Jiang and Z. Li, *Adv. Sci.*, 2021, **8**, 2001938.
- L. Hu, P. L. Chee, S. Sugiarto, Y. Yu, C. Shi, R. Yan, Z. Yao, X. Shi, J. Zhi and D. Kai, *Adv. Mater.*, 2023, **35**, 2205326.
- L. Wang, T. Xu and X. Zhang, *TrAC, Trends Anal. Chem.*, 2021, **134**, 116130.
- M. L. Oyen, *Int. Mater. Rev.*, 2014, **59**, 44–59.
- E. M. Ahmed, *J. Adv. Res.*, 2015, **6**, 105–121.
- H. Yuk, B. Lu and X. Zhao, *Chem. Soc. Rev.*, 2019, **48**, 1642–1667.
- Y. Zhao, X. Fu, B. Liu, J. Sun, Z. Zhuang, P. Yang, J. Zhong and K. Liu, *Sci. China. Mater.*, 2023, **66**, 1934–1940.
- F. Mo, P. Zhou, S. Lin, J. Zhong and Y. Wang, *Adv. Healthcare Mater.*, 2024, **13**, 2401503.
- Y. Huang, M. Xiao, X. Zhou, J. Zhu, Y. Tian, S. Xie, Y. Gong and J. Zhong, *Sens. Actuators, B*, 2025, **431**, 137461.
- Y. Liu, L. Han, S. Lv, T. Jiang, M. Duan, H. Guo, Y. Li, Q. Xie, Y. Chen and D. Wang, *Research*, 2025, **8**, 0714.
- Y. Zhou, Y. Zhao, D. Zhao, X. Guan, K. Zhang, Y. Pi and J. Zhong, *Microsyst. Nanoeng.*, 2025, **11**, 40.
- K. Deligkaris, T. S. Tadele, W. Olthuis and A. van den Berg, *Sens. Actuators, B*, 2010, **147**, 765–774.
- Y. S. Zhang and A. Khademhosseini, *Science*, 2017, **356**, eaaf3627.
- P. Zhou, F. Mo, Z. Ji, J. Yang, H. Du, Z. Wang, H. Haick and Y. Wang, *Sci. Bull.*, 2025, **90**, 1410–1415.
- F. Mo, P. Zhou, S. Lin, J. Zhong and Y. Wang, *Adv. Healthcare Mater.*, 2024, **13**, 2401503.
- P. Zhou, Z. Zhang, F. Mo and Y. Wang, *Adv. Sens. Res.*, 2024, **3**, 2300021.
- F. Mo, Y. Lin, Y. Liu, P. Zhou, J. Yang, Z. Ji and Y. Wang, *Mater. Sci. Eng., R*, 2025, **165**, 100989.
- M. Niu, K. Chen, W. Li, J. Hu, J. Zhang, P. Zhu, Z. Pan and Y. Mao, *J. Mater. Res.*, 2024, **39**, 188–211.
- H. Duan, Y. Zhang, Y. Zhang, P. Zhu and Y. Mao, *Nanomaterials*, 2024, **14**, 1398.
- W. Hu, D. Song, X. Shi and N. Liu, *Sci. Sin.: Chim.*, 2022, **52**, 837–847.
- H. Ding, Y. Gu, Y. Ren, C. Hu, Q. Qiu, D. Wu, J. Mou, Z. Wu and H. Zhou, *J. Mater. Chem. C*, 2024, **9**, 3030–3052.
- Q. Han, C. Zhang, T. Guo, Y. Tian, W. Song, J. Lei, Q. Li, A. Wang, M. Zhang, S. Bai and X. Yan, *Adv. Mater.*, 2023, **35**, 2209606.
- Q. Han, X. Gao, C. Zhang, Y. Tian, S. Liang, X. Li, Y. Jing, M. Zhang, A. Wang and S. Bai, *Adv. Mater.*, 2025, **37**, 2415445.



48 Y. Li, Y. Gu, S. Qian, S. Zheng, Y. Pang, L. Wang, B. Liu, S. Liu and Q. Zhao, *Nano Res.*, 2024, **17**, 5479–5490.

49 Z. Zhang, J. Yang, H. Wang, C. Wang, Y. Gu, Y. Xu, S. Lee, T. Yokota, H. Haick, T. Someya and Y. Wang, *Sci. Adv.*, 2024, **10**, eadj5389.

50 T.-C. Ho, C.-C. Chang, H.-P. Chan, T.-W. Chung, C.-W. Shu, K.-P. Chuang, T.-H. Duh, M.-H. Yang and Y.-C. Tyan, *Molecules*, 2022, **27**, 2902.

51 T. Zhu, Y. Ni, G. M. Biesold, Y. Cheng, M. Ge, H. Li, J. Huang, Z. Lin and Y. Lai, *Chem. Soc. Rev.*, 2023, **52**, 473–509.

52 H. Dechiraju, M. Jia, L. Luo and M. Rolandi, *Adv. Sustainable Syst.*, 2022, **6**, 2100173.

53 S. Chen, Y. Chen, X. Mu, P. Wang, L. Miao, S. Tanemura and H. Cai, *Sustainable Mater. Technol.*, 2023, **36**, e00635.

54 X. Li, Y. Sun, S. Wang, G. Tian, T. Yang, L. Huang, Y. Ao, B. Lan, J. Zhang, T. Xu, Y. Liu, L. Jin, W. Yang and W. Deng, *Chem. Eng. J.*, 2024, **498**, 155195.

55 C. G. Wang, N. E. B. Surat'man, J. J. Chang, Z. L. Ong, B. Li, X. Fan, X. J. Loh and Z. Li, *Chem. – Asian J.*, 2022, **17**, e202200604.

56 A. S. Ivanov, L. V. Pershina, K. G. Nikolaev and E. V. Skorb, *Macromol. Biosci.*, 2021, **21**, 2100117.

57 D. Lu, Z. Zhu, M. Zhu, P. Zhang and X. Xiang, *J. Mater. Chem. A*, 2025, **13**, 427–440.

58 Y. Gao, W. Zhang, L. Li, Z. Wang, Y. Shu and J. Wang, *Chem. Eng. J.*, 2023, **452**, 139248.

59 Z. Luo, W. Li, J. Yan and J. Sun, *Adv. Funct. Mater.*, 2022, **32**, 2203988.

60 Y. Zhao, F. Wang, J. Liu, D. Gan, B. Lei, J. Shao, W. Wang, Q. Wang and X. Dong, *ACS Appl. Mater. Interfaces*, 2023, **15**, 28664–28674.

61 Q. He, Y. Cheng, Y. Deng, F. Wen, Y. Lai and H. Li, *Adv. Funct. Mater.*, 2024, **34**, 2308974.

62 F. Miguel, F. Barbosa, F. C. Ferreira and J. C. Silva, *Gels*, 2022, **8**, 710.

63 M. A. Bhat, R. A. Rather and A. H. Shallal, *Synth. Met.*, 2021, **273**, 116709.

64 B. Zhao, Z. Li, L. Zheng, Z. Ye, Y. Yuan, S. Zhang, B. Liang and T. Li, *Chin. Chem. Lett.*, 2024, **35**, 109810.

65 R. Eivazzadeh-Keihan, E. B. Noruzi, E. Chidar, M. Jafari, F. Davoodi, A. Kashtiaray, M. G. Gorab, S. M. Hashemi, S. Javanshir and R. A. Cohan, *Chem. Eng. J.*, 2022, **442**, 136183.

66 R. Arambula-Maldonado and K. Mequanint, *Mater. Adv.*, 2022, **3**, 5186–5206.

67 Y. Zhao, K. Zhao, R. Qian, Z. Yu and C. Ye, *Chem. Eng. J.*, 2024, 150197.

68 Y. Wang, M. Zhang, Z. Yan, S. Ji, S. Xiao and J. Gao, *Theranostics*, 2024, **14**, 1534.

69 X. Huang, C. Chen, X. Ma, T. Zhu, W. Ma, Q. Jin, R. Du, Y. Cai, M. Zhang, D. Kong, M. Wang, J. A. Ren, Q. Zhang and X. Jia, *Adv. Funct. Mater.*, 2023, **33**, 2302846.

70 J. Dai, D. Ren, S. Zhang, Y. Liu, Y. Xiao, Z. Wang, B. Wang and F. Huang, *ACS Appl. Electron. Mater.*, 2025, **7**, 3125–3134.

71 Y. Ohm, C. Pan, M. J. Ford, X. Huang, J. Liao and C. Majidi, *Nat. Electron.*, 2021, **4**, 185–192.

72 J. Chen, F. Liu, T. Abdiryim and X. Liu, *Adv. Compos. Hybrid Mater.*, 2024, **7**, 35.

73 J. Luo, C. Sun, B. Chang, Y. Jing, K. Li, Y. Li, Q. Zhang, H. Wang and C. Hou, *ACS Nano*, 2022, **16**, 19373–19384.

74 C. Yu, Z. Yue, H. Zhang, M. Shi, M. Yao, Q. Yu, M. Liu, B. Guo, H. Zhang, L. Tian, H. Sun, F. Yao and J. Li, *Adv. Funct. Mater.*, 2023, **33**, 2211023.

75 P. Wang, Y. Lv, J. Duan, G. Sun, C. Meng, Y. Li, S. Guo and T. Zhang, *Nano Energy*, 2025, **136**, 110722.

76 F. Wang, L. Yang, Y. Sun, Y. Cai, X. Xu, Z. Liu, Q. Liu, H. Zhao, C. Ma and J. Liu, *Gels*, 2023, **9**, 323.

77 Z. Wang, L. Chen, Y. Chen, P. Liu, H. Duan and P. Cheng, *Research*, 2020, 2020.

78 Y. Liu, C. Wang, J. Xue, G. Huang, S. Zheng, K. Zhao, J. Huang, Y. Wang, Y. Zhang and T. Yin, *Adv. Healthcare Mater.*, 2022, **11**, 2270092.

79 L. Rong, X. Xie, W. Yuan and Y. Fu, *ACS Appl. Mater. Interfaces*, 2022, **14**, 29273–29283.

80 Y. Shi, Y. Ding, W. Wang and D. Yu, *Colloids Surf. A*, 2023, **675**, 132081.

81 R. Liu, T. Wang, G. Li, Z. Fan, Q. Zhou, K. Wang, P. Li and W. Huang, *Adv. Funct. Mater.*, 2023, **33**, 2214917.

82 Q. Liang, X. Xia, X. Sun, D. Yu, X. Huang, G. Han, S. M. Mugo, W. Chen and Q. Zhang, *Adv. Sci.*, 2022, **9**, 2201059.

83 Q. Wu, A. Chen, Y. Xu, S. Han, J. Zhang, Y. Chen, J. Hang, X. Yang and L. Guan, *Soft Matter*, 2024, **20**, 3666–3675.

84 X. Pan, Q. Wang, P. He, K. Liu, Y. Ni, X. Ouyang, L. Chen, L. Huang, H. Wang and Y. Tan, *ACS Sustainable Chem. Eng.*, 2019, **7**, 7918–7925.

85 M. Lu, L. Shen, H. Su, B. Li, L. Wang and W. W. Yu, *J. Colloid Interface Sci.*, 2025, **684**, 272–282.

86 H. Ma, J. Hou, X. Xiao, R. Wan, G. Ge, W. Zheng, C. Chen, J. Cao, J. Wang, C. Liu, Q. Zhao, Z. Zhang, P. Jiang, S. Chen, W. Xiong, J. Xu and B. Lu, *J. Colloid Interface Sci.*, 2024, **654**, 639–648.

87 J. Lao, Y. Jiao, Y. Zhang, H. Xu, Y. Wang, Y. Ma, X. Feng and J. Yu, *ACS Nano*, 2025, **19**, 7755–7766.

88 J. Zheng, J. Zhou, Y. Zhao, C. Wang, M. Fan, Y. Li, C. Yang and H. Yang, *Biosensors*, 2025, **15**, 177.

89 X. Xia, Q. Liang, X. Sun, D. Yu, X. Huang, S. M. Mugo, W. Chen, D. Wang and Q. Zhang, *Adv. Funct. Mater.*, 2022, **32**, 2208024.

90 H. Xue, D. Wang, M. Jin, H. Gao, X. Wang, L. Xia, D. A. Li, K. Sun, H. Wang, X. Dong, C. Zhang, F. Cong and J. Lin, *Microsyst. Nanoeng.*, 2023, **9**, 79.

91 N. Li, X. Wang, Y. Liu, Y. Li, J. Li, Z. Qin and T. Jiao, *Chem. Eng. J.*, 2024, **483**, 149303.

92 J. Wei, H. Chen, F. Pan, H. Zhang, K. Yang, T. Yuan, Y. Fang, H. Ping, Q. Wang and Z. Fu, *ACS Nano*, 2025, **19**, 15554–15564.

93 X. Zhou, A. Rajeev, A. Subramanian, Y. Li, N. Rossetti, G. Natale, G. A. Lodygensky and F. Cicoira, *Acta Biomater.*, 2022, **139**, 296–306.

94 H. Huang, J. Shen, S. Wan, L. Han, G. Dou and L. Sun, *ACS Appl. Mater. Interfaces*, 2023, **15**, 11549–11562.

95 D. Kim, H. J. Lee, J. Oh, H. Y. Yang, H. J. Park, C. Huh, D. H. Ha, Y. Jun and Y. J. Yun, *J. Mater. Chem. C*, 2025, **13**, 5711–5718.



96 M. Li, W. Li, Q. Guan, J. Lv, Z. Wang, L. Ding, C. Li, E. Saiz and X. Hou, *Device*, 2023, **1**, 1000006.

97 H. Su, L. Mao, X. Chen, P. Liu, J. Pu, Z. Mao, T. Fujiwara, Y. Ma, X. Mao and T. Li, *Adv. Sci.*, 2024, **11**, 2405273.

98 B. Yao, Y. Yan, Q. Cui, S. Duan, C. Wang, Y. Du, Y. Zhao, D. Wu, S. Wu, X. Zhu, T. Hsiai and X. He, *Matter*, 2022, **5**, 4407–4424.

99 C. Liu, Y. Wang, S. Shi, Y. Zheng, Z. Ye, J. Liao, Q. Sun, B. Dang and X. Shen, *ACS Nano*, 2024, **18**, 27420–27432.

100 H. He, H. Li, A. Pu, W. Li, K. Ban and L. Xu, *Nat. Commun.*, 2023, **14**, 759.

101 J. Zhang, Y. Wang, Q. Wei, Y. Wang, M. Lei, M. Li, D. Li, L. Zhang and Y. Wu, *Gels*, 2021, **7**, 216.

102 Z. Chen, Y. Chen, M. S. Hedenqvist, C. Chen, C. Cai, H. Li, H. Liu and J. Fu, *J. Mater. Chem. B*, 2021, **9**, 2561–2583.

103 W. Li, J. Liu, J. Wei, Z. Yang, C. Ren and B. Li, *Adv. Funct. Mater.*, 2023, **33**, 2213485.

104 J. Zhang, Y. Hu, L. Zhang, J. Zhou and A. Lu, *Nano-Micro Lett.*, 2022, **15**, 8.

105 G. Kougkulos, M. Golzio, L. Laudebat, Z. Valdez-Nava and E. Flahaut, *J. Mater. Chem. B*, 2023, **11**, 2036–2062.

106 L. Li, J. Meng, M. Zhang, T. Liu and C. Zhang, *Chem. Commun.*, 2022, **58**, 185–207.

107 Z. Wang, X. Xu, R. Tan, S. Zhang, K. Zhang and J. Hu, *Adv. Funct. Mater.*, 2024, **34**, 2312667.

108 Q. Zhang, H. Lu, G. Yun, L. Gong, Z. Chen, S. Jin, H. Du, Z. Jiang and W. Li, *Adv. Funct. Mater.*, 2024, **34**, 2308113.

109 S. Li, Y. Cong and J. Fu, *J. Mater. Chem. B*, 2021, **9**, 4423–4443.

110 X. Ma, X. Zhou, J. Ding, B. Huang, P. Wang, Y. Zhao, Q. Mu, S. Zhang, C. Ren and W. Xu, *J. Mater. Chem. A*, 2022, **10**, 11823–11853.

111 X. Shi and P. Wu, *Small*, 2021, **17**, 2101220.

112 X. Shi and P. Wu, *Small*, 2021, **17**, 2101220.

113 Y. Gao, K. Wu and Z. Suo, *Adv. Mater.*, 2019, **31**, 1806948.

114 T. Wang, P. Zhang, X. Yang, Y. Zhang, J. Zhang, X. He, P. Gu, X. Gong and Y. Zhao, *Chem. Eng. J.*, 2022, **438**, 135441.

115 Z. Xu, X. Liang, W. Ma, X. An, H. Wu, Q. Zhang and X. Jia, *Adv. Funct. Mater.*, 2024, **34**, 2310233.

116 Y. Liu, P. Wang, X. Su, L. Xu, Z. Tian, H. Wang, G. Ji and J. Huang, *Adv. Mater.*, 2022, **34**, 2108820.

117 G. Bovone, O. Y. Dudaryeva, B. Marco-Dufort and M. W. Tibbitt, *ACS Biomater. Sci. Eng.*, 2021, **7**, 4048–4076.

118 Y. Zhao, S. Song, X. Ren, J. Zhang, Q. Lin and Y. Zhao, *Chem. Rev.*, 2022, **122**, 5604–5640.

119 Y.-W. Lee, S. Chun, D. Son, X. Hu, M. Schneider and M. Sitti, *Adv. Mater.*, 2022, **34**, 2109325.

120 L. Nicolle, C. M. Journot and S. Gerber-Lemaire, *Polymers*, 2021, **13**, 4118.

121 W. Zhang, Y. Zhang, Y. Zhang, Y. Dai, F. Xia and X. Zhang, *J. Mater. Chem. B*, 2021, **9**, 5954–5966.

122 X. Wei, Y. Wang, Y. Liu, K. Ji, K. Li, J. Wang and Z. Gu, *Matter*, 2024, **7**, 826–854.

123 S. Jia, T. Tao, J. Sun, J. Du, Y. Xie, L. Yu, W. Tang, J. Wang and J. Gong, *Small Struct.*, 2023, **4**, 2300139.

124 G. Giordano, M. Carlotti and B. Mazzolai, *Adv. Mater. Technol.*, 2021, **6**, 2100437.

125 T. Cheng, Y. Z. Zhang, S. Wang, Y. L. Chen, S. Y. Gao, F. Wang, W. Y. Lai and W. Huang, *Adv. Funct. Mater.*, 2021, **31**, 2101303.

126 Y. Zhang, X. Sun, Y. Ye, H. Oguzlu, Y. Zhu, J. Zhu, K. Le, P. Yang and F. Jiang, *Mater. Today*, 2024, **74**, 67–76.

127 W. Li, S. Zheng, X. Zou, Y. Ren, Z. Liu, W. Peng, X. Wang, D. Liu, Z. Shen, Y. Hu, J. Guo, Z. Sun and F. Yan, *Adv. Funct. Mater.*, 2022, **32**, 2207348.

128 R. Ji, S. Yan, Z. Zhu, Y. Wang, D. He, K. Wang, D. Zhou, Q. Jia, X. Wang, B. Zhang, C. Shi, T. Xu, R. Wang, R. Wang and Y. Zhou, *Adv. Sci.*, 2024, **11**, 2401869.

129 J. Yang, Z. Zhang, P. Zhou, Y. Zhang, Y. Liu, Y. Xu, Y. Gu, S. Qin, H. Haick and Y. Wang, *Nanoscale*, 2023, **15**, 3051–3078.

130 Y. Wang, *Soft. Sci.*, 2024, **4**, 5.

131 Y. Wang, H. Haick, S. Guo, C. Wang, S. Lee, T. Yokota and T. Someya, *Chem. Soc. Rev.*, 2022, **51**, 3759–3793.

132 S. Cheng, Z. Lou, L. Zhang, H. Guo, Z. Wang, C. Guo, K. Fukuda, S. Ma, G. Wang, T. Someya, H.-M. Cheng and X. Xu, *Adv. Mater.*, 2023, **35**, 2206793.

133 S. Wei, R. Yin, T. Tang, Y. Wu, Y. Liu, P. Wang, K. Wang, M. Mei, R. Zou and X. Duan, *ACS Nano*, 2019, **13**, 7920–7929.

134 B. Khan, Z. Riaz and B. L. Khoo, *Mater. Sci. Eng., R*, 2024, **159**, 100804.

135 P. A. Moreno-Sánchez, G. García-Isla, V. D. Corino, A. Vehkaoja, K. Brukamp, M. Van Gils and L. Mainardi, *Comput. Biol. Med.*, 2024, 108235.

136 J. C. Hwang, M. Kim, S. Kim, H. Seo, S. An, E. H. Jang, S. Y. Han, M. J. Kim, N. K. Kim and S.-W. Cho, *Sci. Adv.*, 2022, **8**, eabq0897.

137 S.-H. Sunwoo, S. I. Han, C. S. Park, J. H. Kim, J. S. Georgiou, S.-P. Lee, D.-H. Kim and T. Hyeon, *Nat. Rev. Bioeng.*, 2024, **2**, 8–24.

138 B. Pan, F. Xiong, J. Wang, J. Fu, Y. Ding, R. Qin and S. Li, *Talanta*, 2025, 127591.

139 Y. Du, J. H. Kim, H. Kong, A. A. Li, M. L. Jin, D. H. Kim and Y. Wang, *Adv. Healthcare Mater.*, 2024, **13**, 2303461.

140 S. Tang, D. Sha, Z. He, X. Chen, Y. Ma, C. Liu and Y. Yuan, *Adv. Healthcare Mater.*, 2023, **12**, 2300475.

141 Y. Zhang, Q. Tang, J. Zhou, C. Zhao, J. Li and H. Wang, *ACS Biomater. Sci. Eng.*, 2023, **10**, 191–218.

142 X. Shi, H. Yu, Z. Tang, S. Lu, M. You, H. Yin and Q. Chen, *Sci. China Technol. Sci.*, 2024, **67**, 3136–3151.

143 G. Yang, Z. Lan, H. Gong, J. Wen, B. Pang, Y. Qiu, Y. Zhang, W. Guo, T. Bu, B. Xie and H. Wu, *Adv. Funct. Mater.*, 2025, **35**, 2417841.

144 S. Chen, Q. Ouyang, X. Meng, Y. Yang, C. Li, X. Miao, Z. Chen, G. Zhao, Y. Lei, B. Ghanem, S. Gautam, J. Cheng and Z. Yan, *Sci. Adv.*, 2025, **11**, eadv2406.

145 D. Farina, R. Merletti and R. M. Enoka, *J. Appl. Physiol.*, 2004, **96**, 1486–1495.

146 H. Wang, Q. Ding, Y. Luo, Z. Wu, J. Yu, H. Chen, Y. Zhou, H. Zhang, K. Tao and X. Chen, *Adv. Mater.*, 2024, **36**, 2309868.

147 S. Yang, J. Cheng, J. Shang, C. Hang, J. Qi, L. Zhong, Q. Rao, L. He, C. Liu and L. Ding, *Nat. Commun.*, 2023, **14**, 6494.



148 J. Wu, J. Xian, C. He, H. Lin, J. Li and F. Li, *Adv. Mater.*, 2024, **36**, 2405372.

149 Y. Zhang, L. Chen, M. Xie, Z. Zhan, D. Yang, P. Cheng, H. Duan, Q. Ge and Z. Wang, *Mater. Today Phys.*, 2022, **27**, 100794.

150 J. Park, Y. Lee, S. Cho, A. Choe, J. Yeom, Y. G. Ro, J. Kim, D.-H. Kang, S. Lee and H. Ko, *Chem. Rev.*, 2024, **124**, 1464–1534.

151 H. Yuk, J. Wu and X. Zhao, *Nat. Rev. Mater.*, 2022, **7**, 935–952.

152 J.-W. Lee, M.-J. Shin, M.-H. Jang, W.-B. Jeong and S.-J. Ahn, *Med. Eng. Phys.*, 2021, **98**, 65–72.

153 V. Alcan and M. Zinnuroğlu, *Turk. J. Med. Sci.*, 2023, **53**, 1019–1031.

154 Q. Liu, X. Xu, Y. Zhang, L. Liang, B. Zhang and S. Chen, *Chem. Eng. J.*, 2025, **509**, 161207.

155 S. Roubert Martinez, P. Le Floch, J. Liu and R. D. Howe, *Adv. Healthcare Mater.*, 2023, **12**, 2202661.

156 R. Wan, J. Yu, Z. Quan, H. Ma, J. Li, F. Tian, W. Wang, Y. Sun, J. Liu and D. Gao, *Chem. Eng. J.*, 2024, **490**, 151454.

157 R. Wan, S. Liu, Z. Li, G. Li, H. Li, J. Li, J. Xu and X. Liu, *J. Colloid Interface Sci.*, 2025, **677**, 198–207.

158 T. Li, H. Qi, C. Zhao, Z. Li, W. Zhou, G. Li, H. Zhuo and W. Zhai, *Nat. Commun.*, 2025, **16**, 88.

159 J. Gavvala, N. Abend, S. LaRoche, C. Hahn, S. T. Herman, J. Claassen, M. Macken, S. Schuele, E. Gerard and C. C. E. M. R. Consortium, *Epilepsia*, 2014, **55**, 1864–1871.

160 C. De Gans, P. Burger, E. Van den Ende, J. Hermanides, P. Nanayakkara, R. Gemke, F. Rutters and D. Stenvers, *Sleep Med. Rev.*, 2024, 101951.

161 M. Mohamed, N. Mohamed and J. G. Kim, *Biosensors*, 2023, **13**, 1019.

162 J.-C. Hsieh, W. He, D. Venkatraghavan, V. B. Koptelova, Z. J. Ahmad, I. Pyatnitskiy, W. Wang, J. Jeong, K. K. W. Tang and C. Harmeier, *Device*, 2024, **2**, 100182.

163 X. Li, Y. Zhang, P. Tiwari, D. Song, B. Hu, M. Yang, Z. Zhao, N. Kumar and P. Marttinen, *ACM Comput. Surv.*, 2022, **55**, 1–57.

164 G. Yang, K. Zhu, W. Guo, D. Wu, X. Quan, X. Huang, S. Liu, Y. Li, H. Fang and Y. Qiu, *Adv. Funct. Mater.*, 2022, **32**, 2200457.

165 M. Hu, J. Ren, Y. Pan, L. Cheng, X. Xu, C. L. Tan, H. Sun, Y. Shi and S. Yan, *Adv. Funct. Mater.*, 2024, **34**, 2407926.

166 G. Li, Y. Liu, Y. Chen, M. Li, J. Song, K. Li, Y. Zhang, L. Hu, X. Qi and X. Wan, *J. Neural Eng.*, 2023, **20**, 026017.

167 J. Liu, S. Lin, W. Li, Y. Zhao, D. Liu, Z. He, D. Wang, M. Lei, B. Hong and H. Wu, *Research*, 2022, **2022**, 9830457.

168 W. U. Khan, Z. Shen, S. M. Mugo, H. Wang and Q. Zhang, *Chem. Soc. Rev.*, 2025, **54**, 2832–2880.

169 Q. Han, C. Zhang, T. Guo, Y. Tian, W. Song, J. Lei, Q. Li, A. Wang, M. Zhang and S. Bai, *Adv. Mater.*, 2023, **35**, 2209606.

170 C. Wang, H. Wang, B. Wang, H. Miyata, Y. Wang, M. O. G. Nayyem, J. J. Kim, S. Lee, T. Yokota, H. Onodera and T. Someya, *Sci. Adv.*, 2022, **8**, eab01396.

171 L. Li, X. Ye, Z. Ji, M. Zheng, S. Lin, M. Wang, J. Yang, P. Zhou, Z. Zhang, B. Wang, H. Wang and Y. Wang, *Small*, 2025, **21**, 2407996.

172 G. Fang, X. Yang, Q. Wang, A. Zhang and B. Tang, *Mater. Sci. Eng. C*, 2021, **127**, 112212.

173 R. Lev and D. Seliktar, *J. Royal Soc. Interface*, 2018, **15**, 20170380.

174 N. A. Alba, R. J. Sclabassi, M. Sun and X. T. Cui, *IEEE Trans. Neural Syst. Rehabil. Eng.*, 2010, **18**, 415–423.

175 J. S. Blasco, E. Iáñez, A. Ubeda and J. M. Azorín, *Expert Syst. Appl.*, 2012, **39**, 7908–7918.

176 G. Perale, F. Rossi, E. Sundstrom, S. Bacchigia, M. Masi, G. Forloni and P. Veglianese, *ACS Chem. Neurosci.*, 2011, **2**, 336–345.

177 K. Pradhan, G. Das, J. Khan, V. Gupta, S. Barman, A. Adak and S. Ghosh, *ACS Chem. Neurosci.*, 2018, **10**, 1535–1543.

178 V. Martínez-Cagigal, J. Thielen, E. Santamaría-Vazquez, S. Pérez-Velasco, P. Desain and R. Hornero, *J. Neural Eng.*, 2021, **18**, 061002.

179 J. Sosulski and M. Tangermann, *J. Neural Eng.*, 2022, **19**, 066001.

180 M. Zheng, L. Li, X. Ye, Z. Ji, Y. Wang, Z. Wang, S. Lin, M. Wang, W. Yan, J. Yang, P. Zhou, Y. Zhang, R. Niu, H. Haick and Y. Wang, *Chem. Eng. J.*, 2025, **512**, 162451.

181 X. Pan, J. Guan, S. Cao, X. Ma, Y. Ni and Q. Wang, *J. Colloid Interface Sci.*, 2025, **680**, 753–761.

